



Structure-Function Discrepancy: Inhomogeneity and Delays in Synchronized Neural Networks

Robert Ton^{1,2*}, Gustavo Deco^{2,3}, Andreas Daffertshofer¹

1 MOVE Research Institute Amsterdam, VU University, Amsterdam, The Netherlands, **2** Center for Brain and Cognition, Computational Neuroscience Group, Universitat Pompeu Fabra, Barcelona, Spain, **3** Institutió Catalana de la Recerca i Estudis Avançats (ICREA), Universitat Pompeu Fabra, Barcelona, Spain

Abstract

The discrepancy between structural and functional connectivity in neural systems forms the challenge in understanding general brain functioning. To pinpoint a mapping between structure and function, we investigated the effects of (in)homogeneity in coupling structure and delays on synchronization behavior in networks of oscillatory neural masses by deriving the phase dynamics of these generic networks. For homogeneous delays, the structural coupling matrix is largely preserved in the coupling between phases, resulting in clustered stationary phase distributions. Accordingly, we found only a small number of synchronized groups in the network. Distributed delays, by contrast, introduce inhomogeneity in the phase coupling so that clustered stationary phase distributions no longer exist. The effect of distributed delays mimicked that of structural inhomogeneity. Hence, we argue that phase (de-)synchronization patterns caused by inhomogeneous coupling cannot be distinguished from those caused by distributed delays, at least not by the naked eye. The here-derived analytical expression for the effective coupling between phases as a function of structural coupling constitutes a direct relationship between structural and functional connectivity. Structural connectivity constrains synchronizability that may be modified by the delay distribution. This explains why structural and functional connectivity bear much resemblance albeit not a one-to-one correspondence. We illustrate this in the context of resting-state activity, using the anatomical connectivity structure reported by Hagmann and others.

Citation: Ton R, Deco G, Daffertshofer A (2014) Structure-Function Discrepancy: Inhomogeneity and Delays in Synchronized Neural Networks. *PLoS Comput Biol* 10(7): e1003736. doi:10.1371/journal.pcbi.1003736

Editor: Jean Daunizeau, Brain and Spine Institute (ICM), France

Received: October 18, 2013; **Accepted:** June 6, 2014; **Published:** July 31, 2014

Copyright: © 2014 Ton et al. This is an open-access article distributed under the terms of the Creative Commons Attribution License, which permits unrestricted use, distribution, and reproduction in any medium, provided the original author and source are credited.

Funding: This work was funded by ERC Advanced Grant: DYSTRUCTURE (n. 295129), by the Spanish Research Project SAF2010-16085 and by the CONSOLIDER-INGENIO 2010 Program CSD2007-00012, and the FP7-ICT BrainScales. The funders had no role in study design, data collection and analysis, decision to publish, or preparation of the manuscript.

Competing Interests: The authors have declared that no competing interests exist.

* Email: r.ton@vu.nl, robert.ton@upf.edu

Introduction

Much of the current focus in the empirical study of large-scale neuronal networks has been on their intrinsic activity and the degree to which the coherent patterns of this intrinsic activity reflect anatomy. The use of fMRI and diffusion spectrum imaging has allowed for a comprehensive evaluation of the structure-function map of resting-state networks (RSNs). In fMRI the spatial patterns of spontaneous changes in blood oxygenation level-dependent signals seem to reflect the generating neural architecture of RSNs. Despite the very slow changes of these signals, Biswal and co-workers [1] defined RSNs as networks of brain areas that exhibit *temporally coherent activity* in the absence of identifiable externally imposed or measurable events. More recently, RSNs penetrated the field of encephalography [2,3]. For M/EEG, locally synchronized neural activity is considered to yield macroscopic oscillations that provide a basis for defining functional brain networks [4]. In most studies, structural connectivity is considered a good predictor of functional connectivity [5,6]: Structural connectivity agrees with the anatomical connections between network nodes and functional connectivity covers the statistical relationship of nodal activity.

The predictive value of structure for function found support in recent modeling work using full brain systems with realistic anatomy, which demonstrated the structural dependency of

functional network configurations [7]. There, functional connectivity has been estimated between all nodes over several hundred seconds of simulated time yielding the pattern of functional connectivity over this time window that largely reproduced the structural connectivity. At smaller time windows, however, shorter-living patterns of functional connectivity emerged that had not been predicted by anatomy. To understand this discrepancy we investigated effects of time delays vis-à-vis effects of structural inhomogeneity on synchronization patterns of neuronal networks.

Delays are inherent in neuronal networks due to finite conduction velocities [8] and synaptic transmission [9]. Ignoring delays may be a valid starting point for mathematical analysis but when doing so one runs the risk of losing biological plausibility. However, incorporating delays in oscillatory networks does come with immense challenges. Already for low-dimensional oscillatory systems (or for high-dimensional ones with strong symmetry) the presence of delays is known to change the dynamical repertoire significantly [10,11]. Yeung and Strogatz showed for very large networks how time delays can alter synchronization properties, even if the structure is isotropic and homogeneous [12]; see also [13,14]. Numerical assessments revealed similar results for biologically motivated and hence more inhomogeneous connectivities. Delays seem to be crucial in establishing the spatio-temporally organized fluctuations typically observed in resting

Author Summary

Separating the time scale of oscillations from that of the phase dynamics allowed for reducing a network of coupled neural mass models to a system of phase oscillators. We studied the dynamics of networks of phases and their synchronization characteristics as being seminal for functional neural networks. We put particular focus on effects of time delays in the coupling on the network dynamics and contrasted that to effects due to altered structural connectivity. Does neuroanatomical structure prescribe all the macroscopic activity patterns that we observe through electrophysiological brain recordings? We found that heterogeneity in structural coupling and distributed delays have equivalent effects on the shape of phase distributions, i.e., on functional connectivity. The contribution of changes in structural connectivity to network synchronization can therefore not readily be distinguished from that of distributed delays. Interestingly, the emergence of phase clusters in networks requires a subtle interplay between coupling and delays, which may form a window into disentangling structural effects from those induced by delay distributions. Therefore, when investigating neural network behavior, both structural connectivity and delay distribution should be addressed.

state brain recordings [15–17]. In the present study we sought to tackle this issue and separated the effect of time delays from that of inhomogeneous connectivity by studying networks consisting of distinct neural masses. Neural mass models offer a low-dimensional description of the dynamics of a large neuronal population and exist in a variety of forms [18]. We chose for Freeman’s seminal model [19–21], since it covers the dynamics of mean membrane potential changes that relate closely to encephalographic signals. A network of such entities may constitute RSNs if we regard the neural masses to be representative of individual brain areas.

Throughout the paper we describe functional connectivity by means of phase synchronization whose dynamics can be estimated in voltage-based and firing-rate models using a combination of *rotating wave* and *slowly varying amplitude* approximations, or in brief *averaging*, see [22,23]. In the *Methods* section this combination of approximations is briefly summarized for Freeman neural mass models in the oscillatory regime. Central outcome measure is thus the phase dynamics of the individual nodes in the network or, to be more precise, the density of the nodes’ phases as a function of time, often also referred as time-dependent *population distributions*. We note that we applied this approach before to instantaneously coupled Wilson-Cowan firing rate models [24] (see also [25]) but, as said, we here chose for the Freeman model for an easier comparison with M/EEG studies. For coupled Freeman models we could analytically determine the corresponding stationary distributions even in the presence of delays and inhomogeneous coupling between neural masses. We could not only prove the existence of these solutions, but we were also able to determine the loss of stability of the desynchronized state as soon as the overall coupling strength exceeded a critical value. More complicated scenarios including biological plausible anatomical adjacencies were treated numerically to illustrate the non-trivial relationship between structural and functional connectivity.

Results

We considered a set of N coupled neural masses whose mean membrane potentials V_k follow the dynamics

$$\begin{aligned} \dot{V}_k = & -(\alpha_k + \beta_k)\dot{V}_k - \alpha_k \beta_k V_k + \alpha_k \beta_k q_k + \\ & \alpha_k \beta_k \sum_{l=1}^N C_{kl} [W(t) * S[V_l(t - \tau_{kl})]] . \end{aligned} \quad (1)$$

In this expression α_k and β_k represent mean rise and decay times of neural responses in population k , q_k stands for an external input, and $S[\cdot]$ denotes a sigmoidal activity function covering the effects of pulse-coupled neurons in populations $l = 1 \dots N$ [19,26]. Corresponding mean activities V_l arrive at population k after yet arbitrary delays τ_{kl} . The structural connectivity matrix C_{kl} served to introduce both excitatory and inhibitory connections in the thus asymmetric coupling; see Fig 1A. We first considered the case in which a large degree of homogeneity was present in C_{kl} to define a ‘baseline’. Subsequently we introduced inhomogeneity to mimic, e.g., the sparse connectivity presumably underlying RSNs. Two seminal coupling schemes are sketched in Fig 1. Excitatory and inhibitory populations were always properly balanced to stabilize oscillatory behavior [27,28]. This translates to the condition that at least one pair of the eigenvalues of the linearized system around the fixed points $V_k^{(0)}, U_l^{(0)}$ must be imaginary with positive real part. From the *Methods* section it follows that the considered coupling schemes did satisfy this condition.

For the convolution we chose an exponentially decaying kernel W

$$W(t) = \begin{cases} \gamma e^{-\gamma t} & \text{for } t \geq 0 \\ 0 & \text{otherwise} \end{cases}, \quad (2)$$

to represent the dynamics at the synaptic junction. In the particular case of infinitesimal memory, i.e. for $\gamma \rightarrow \infty$, we found the corresponding phase dynamics by transforming the neural mass dynamics to polar coordinates around an unstable focus, i.e. $V_k \rightarrow V_k^{(0)} + R_k \cos(\Omega t + \phi_k)$; R_k denotes the amplitude of oscillation and ϕ_k its phase corresponding to the central frequency Ω . Subsequently, we averaged the dynamics over one period $2\pi/\Omega$. We assumed that the characteristic times of amplitude and phase

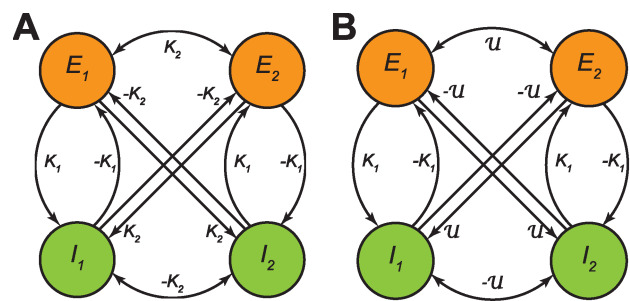


Figure 1. Structural connectivity in the case of two coupled pairs of excitatory/inhibitory neural masses. A: Homogeneous coupling with coupling matrix $C_{kl}^{(hom)}$. **B:** Inhomogeneous coupling using the coupling matrix $C_{kl}^{(inh)}$. In both cases excitatory/inhibitory-pairs have a symmetric ‘internal’ coupling with strength $\pm K_1$ but the coupling between these pairs differs. In A the between-pair coupling is homogeneous at strength K_2 whilst in B the between-pair coupling may differ across pairs; i.e. it is randomly chosen from a certain distribution U with the constraint that inhibitory units map (on average) with negative and excitatory with positive coupling strength. See text for more details and Figs 7 and 8A for the more complicated coupling schemes employed below.
doi:10.1371/journal.pcbi.1003736.g001

dynamics are significantly larger than the period $2\pi/\Omega$, i.e. amplitude and phase dynamics are slow compared to the oscillation. We also assumed the time delays to be of the same order of magnitude or smaller than the period. As a result the delays τ_{kl} reduced to mere phase shifts Δ_{kl} and the phase dynamics became

$$\dot{\phi}_k = \omega_k - \alpha_k \beta_k \sum_{l=1}^N D_{kl} \sin(\phi_l - \phi_k + \Delta_{kl}) \quad (3)$$

with $D_{kl} = \frac{1}{2\Omega} \frac{R_l}{R_k} S' [V_l^{(0)}] C_{kl}$.

In the dynamics (3) the frequencies obeyed the form $\omega_k = \frac{\alpha_k \beta_k - \Omega^2}{2\Omega}$ and the phase shifts read $\Delta_{kl} = \frac{\pi}{2} - \Omega \tau_{kl}$. As said, delays could be transformed to phase shifts due to a time scale separation in the system, i.e. the phase dynamics was set sufficiently slow compared to the oscillation and the delays τ_{kl} were up to the same order of magnitude as one period of oscillation (cf. Fig 2).

At first glance the dynamics (3) seemed to largely resemble the Kuramoto network of phase oscillators that is well known for its bifurcation scheme from desynchronized to synchronized states. The latter, i.e. the fully synchronized state, would imply large-scale — if not whole-brain — synchronization, which, apart for very pathological cases, is not observed experimentally. Nonetheless we considered linking our study to Kuramoto's profound work to be very insightful, as understanding the Kuramoto network is essential for understanding synchronizability in our more general framework. A closer look revealed that, although similar, (3) differs from the Kuramoto network in two important aspects. First, in the phase dynamics the coupling is given by D_{kl} , which in general is not entirely homogeneous as in Kuramoto's case. This expression for D_{kl} agrees with the previously derived phase dynamics of coupled Wilson-Cowan oscillators in that the amplitude relation R_l/R_k between nodes l and k affects the corresponding (relative) phase [24]. Second, the finite delay τ_{kl} yields a non-trivial phase shift $\Delta_{kl} = \frac{\pi}{2} - \Omega \tau_{kl}$. This phase shift might alter the spectrum of phase synchronization entirely; see, e.g., [29,30] for the case.

Instead of studying the mere collection of phases $\{\phi_1, \dots, \phi_N\}$ we investigated the dynamics of their probability density

$\mathcal{P} = \mathcal{P}(\phi_1, \dots, \phi_N, t)$, because it forms a proper measure of synchronization. To explain: Synchronization around a certain phase value θ manifests itself as a peak in the probability density around that value, i.e. a phase cluster around θ . For our set of Freeman neural masses we found that the phase distribution follows the dynamics

$$\dot{\mathcal{P}} = - \sum_{k=1}^N \frac{\partial}{\partial \phi_k} \left[\omega_k - \alpha_k \beta_k \sum_{l=1}^N D_{kl} \sin(\phi_l - \phi_k + \Delta_{kl}) \right] \mathcal{P}. \quad (4)$$

This is the continuity equation, which equals the zero-noise limit of the corresponding Fokker-Planck equation when presuming ergodicity and very large networks ($N \rightarrow \infty$). Despite the presence of delays τ_{kl} we here succeeded to specify stationary solutions $\mathcal{P}_{\text{stat}}(\phi_1, \dots, \phi_N)$. Crucial in finding these solutions was the fact that they can always be written as a mere sum of distinct clustered states, i.e. they always obey the form $\mathcal{P}_{\text{stat}} = \frac{1}{N} \sum_{k=1}^N \delta(\phi_k - \theta_k)$, because the network has a countable number of nodes. Put differently, the phase distribution contains clusters centered around $\theta_1, \theta_2, \dots, \theta_N$. In general, the real number of clusters is given by the number M of distinguishable centroids θ_k ; we always consider $M \leq N$. The number M strongly depends on the distribution of delays and/or inhomogeneity of the coupling matrix C_{kl} or strictly speaking of the effective coupling D_{kl} .

In order to illustrate stationary solutions of (4) we first specified the coupling matrix C_{kl} to be either homogeneous or inhomogeneous. In both cases we labeled excitatory and inhibitory populations by \mathcal{E} and \mathcal{I} , respectively, and defined the corresponding sets $\mathcal{E} = \left\{ k = 1, \dots, \frac{N}{2} \right\}$ and $\mathcal{I} = \left\{ k = \frac{N}{2} + 1, \dots, N \right\}$. As mentioned above we guaranteed throughout analysis that all excitatory populations had an inhibitory counterpart generating and stabilizing oscillatory activity at around the central frequency Ω [27,28]. For the sake of simplicity we ignored self-coupling of neuronal populations. The stationary phase distribution could thus be written as

$$\mathcal{P}_{\text{stat}} = \mathcal{P}_{\text{stat}}(\phi_{\mathcal{E}}, \phi_{\mathcal{I}}) = \frac{1}{N} \sum_{k \in \mathcal{E}} \delta(\phi_k - \theta_k) + \frac{1}{N} \sum_{k \in \mathcal{I}} \delta(\phi_k - \theta_k). \quad (5)$$

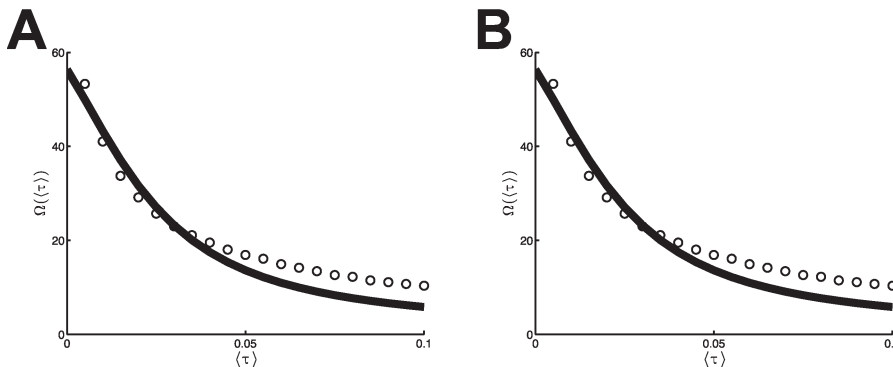


Figure 2. Frequency and period as a function of delay. **A:** Oscillation frequency Ω . **B:** Period $2\pi/\Omega$. The analytical estimate under small-delay approximation (see *Methods*) is displayed as a solid line; results of numerical simulations of the dynamics (1) as dots (\circ). Simulations were performed for homogeneous coupling $C_{kl}^{(\text{hom})}$ with within-pair coupling $K_1 = 1$, between-pair coupling strength $K_2 = 0.2$, and distributed delays τ_{kl} ; see text for details. The presence of between-pair coupling K_2 and even heterogeneity in coupling, $C_{kl}^{(\text{hom})} \rightarrow C_{kl}^{(\text{inh})}$, did not yield qualitatively different results.

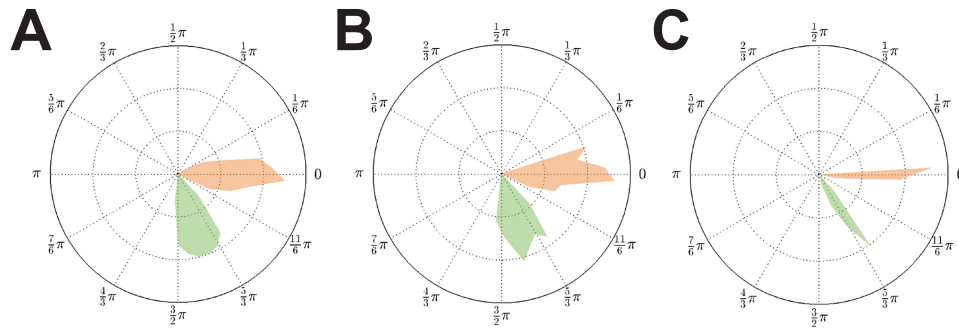


Figure 3. Phase distributions for strong coupling ($K_2=0.6$) and equal delays. A: Vanishing delay ($\tau=0$). **B:** Fixed finite delay $\tau=0.05$. **C:** Fixed finite delay $\tau=0.2$. In all cases synchronized solutions $\mathcal{P}_{\text{stat},2}$ can be seen and appeared to be the only stable solution in the case of strong coupling $K_2=0.6$. Phase distributions were obtained from simulations of the original system (1), where phases were extracted using the Hilbert transforms of $V_k(t)$; see *Methods* section. In this and all subsequent figures excitatory phases ϕ_E are depicted in orange and inhibitory phases ϕ_I in green. Radial axes are normalized.
doi:10.1371/journal.pcbi.1003736.g003

Homogeneous coupling

In the homogeneous case we employed the coupling scheme sketched in Fig 1A. Excitatory and inhibitory populations were fully connected (apart from self-coupling) with coupling values K_1 and K_2 discriminating within-pair and between-pair coupling. For the numerical assessment we always fixed the within-pair coupling to $K_1=1$. In more detail, we chose the overall homogeneous coupling matrix as

$$C_{kl}^{(\text{hom})} = \begin{bmatrix} C_{\mathcal{E}\mathcal{E}}^{(\text{hom})} & C_{\mathcal{E}\mathcal{I}}^{(\text{hom})} \\ C_{\mathcal{I}\mathcal{E}}^{(\text{hom})} & C_{\mathcal{I}\mathcal{I}}^{(\text{hom})} \end{bmatrix}$$

with sub-population connectivities

$$C_{\mathcal{E}\mathcal{E}}^{(\text{hom})} = \begin{bmatrix} 0 & \frac{2K_2}{N} \\ \frac{2K_2}{N} & 0 \end{bmatrix} = -C_{\mathcal{I}\mathcal{I}}^{(\text{hom})}$$

and

$$C_{\mathcal{I}\mathcal{E}}^{(\text{hom})} = \begin{bmatrix} K_1 & \frac{2K_2}{N} \\ \frac{2K_2}{N} & K_1 \end{bmatrix} = -C_{\mathcal{E}\mathcal{I}}^{(\text{hom})}.$$

In the absence of delays, i.e. for $\tau_{kl}=0$ ($\Delta_{kl}=\frac{\pi}{2}$) and sufficiently strong coupling K_2 we found robust distributions with $M=2$ phase clusters, one containing all the excitatory populations and one all the inhibitory ones:

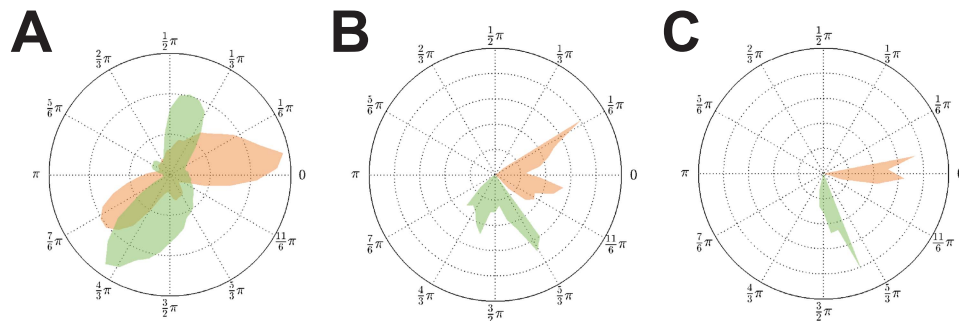


Figure 4. Phase distributions for weak coupling ($K_2=0.2$) and equal delays. A: Vanishing delay ($\tau=0$). **B:** Fixed finite delay $\tau=0.05$. **C:** Fixed finite delay $\tau=0.2$. As for strong coupling we found synchronized solutions $\mathcal{P}_{\text{stat},2}$ in the weak coupling case $K_2=0.2$. In addition solutions $\mathcal{P}_{\text{stat},4}$ were also present. The number of clusters did depend on the delay value τ . That is, altering the delay from $\tau=0$ to $\tau=0.2$ caused a switch in stability between these two solutions. Since for $\tau=0.05$ the two clusters within an \mathcal{E}/\mathcal{I} -group only showed a small phase difference, we conjecture that $\tau=0.05$ is close to the critical value of this bifurcation parameter.
doi:10.1371/journal.pcbi.1003736.g004

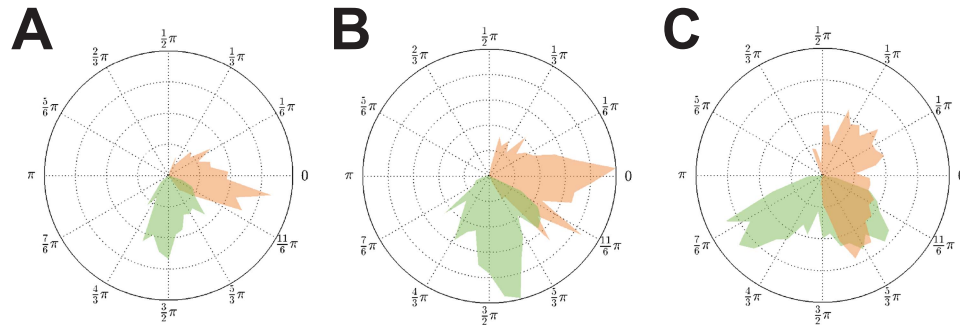


Figure 5. Phase distributions for different coupling strengths and distributed delays. **A:** $K_2=0.6$, $\tau_{kl} \sim \mathcal{U}(0,0.05)$. **B:** $K_2=0.6$, $\tau_{kl} \sim \mathcal{U}(0,0.2)$. **C:** $K_2=0.2$, $\tau_{kl} \sim \mathcal{U}(0,0.05)$. The effect of a delay distribution and consequently the presence of $M=N$ centroid phase values θ_k manifested itself as a widening of the phase distribution compared to the constant delay cases in Fig 4. Narrow delay distributions with $\tau_{kl} \sim \mathcal{U}(0,0.05)$, i.e. the τ_{kl} were randomly drawn from a uniform distribution over the interval $[0,0.05]$, yielded comparably narrow phase distributions located around two narrow peaks (peaks representing the \mathcal{E} - and \mathcal{I} -populations; (A)). Increasing the width of the delay distribution to $\tau_{kl} \sim \mathcal{U}(0,0.2)$ (B) had a very similar effect as lowering the coupling strength $K_2=0.2$ (C): in both cases the phase distribution widened substantially. doi:10.1371/journal.pcbi.1003736.g005

$$\mathcal{P}_{\text{stat},2}(\phi_{\mathcal{E}}, \phi_{\mathcal{I}}) = \frac{1}{2} \delta(\phi_{\mathcal{E}} - \theta_{\mathcal{E}}) + \frac{1}{2} \delta(\phi_{\mathcal{I}} - \theta_{\mathcal{I}}).$$

An example of this solution is illustrated in Fig 3A; the remaining panels in that figure refer to cases of non-vanishing delay that will be summarized below. We note that due to symmetry the homogeneous case with $\tau_{kl}=0$ can be readily transformed, proving its resemblance with the Kuramoto network [31]. The somewhat lengthy analytic derivations are given in the *Methods* section.

Next to the homogeneously synchronized state $\mathcal{P}_{\text{stat},2}$ we found a solution with $M=4$ phase clusters given by

$$\mathcal{P}_{\text{stat},4}(\phi_{\mathcal{E}}, \phi_{\mathcal{I}}) = \frac{1}{4} \delta(\phi_{\mathcal{E}} - \theta_{\mathcal{E},1}) + \frac{1}{4} \delta(\phi_{\mathcal{E}} - \theta_{\mathcal{E},2}) + \frac{1}{4} \delta(\phi_{\mathcal{I}} - \theta_{\mathcal{I},1}) + \frac{1}{4} \delta(\phi_{\mathcal{I}} - \theta_{\mathcal{I},2}).$$

Again we refer to the *Methods* for the analytical treatment with respect to the existence of this stationary solution; see Figs 3A and 4A for the corresponding numerical assessments. The specific form of the dynamics (3) and (4) already suggested that $\tau_{kl}=0$ is just a special case of $\tau_{kl}=\tau \neq 0$. We therefore expected the existence of the solutions above not to be affected by introducing homogeneous, finite delays $\tau_{kl}=\tau \neq 0$, even if this appeared somewhat counterintuitive. In fact, numerics confirmed this expectation as displayed in Figs 3B, 3C, 4B and 4C.

The introduction of distributed delays τ_{kl} instead of a single τ changed results profoundly. To exemplify this, we distributed delays τ_{kl} by drawing them at random from a uniform distribution over a certain interval. Recall that according to the transformation from (1) to (3), a distribution of delays τ_{kl} generally implies an equivalent distribution of phase shifts Δ_{kl} . If Δ_{kl} differed for all populations k and l , the stationary solution $\mathcal{P}_{\text{stat}}(\phi_1, \dots, \phi_N)$ of the continuity equation (4) required the presence of many distinct phase clusters. We could prove the existence of that set and,

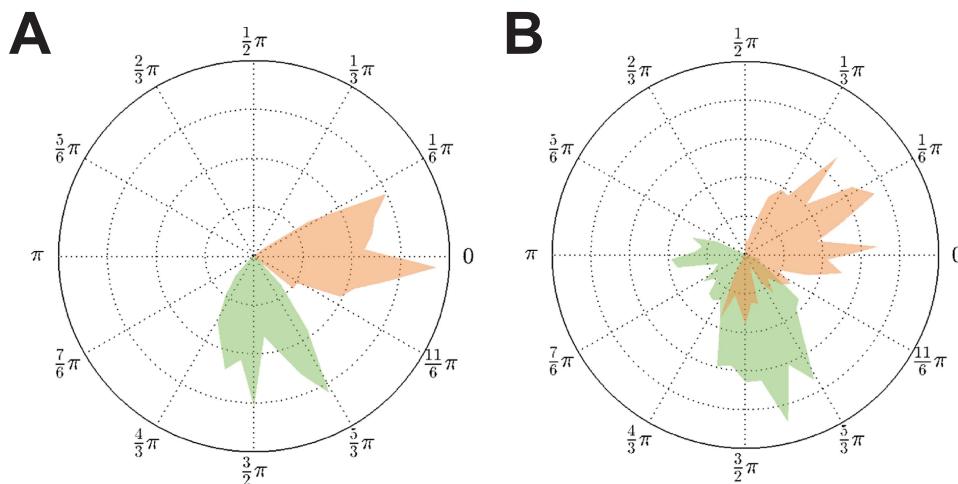


Figure 6. Phase distributions in the presence of inhomogeneous coupling $C_{kl}^{(\text{inh})}$. **A:** Strong coupling ($K_2=0.6$). **B:** Weak coupling ($K_2=0.2$). As predicted by the phase derivation (9), inhomogeneity in the coupling matrix resulted in similar behavior as a distribution in delays; compare Figs 5A and 5C with panels Fig. 6A and 6B respectively. For reasonably weak coupling we found a widening of the phase distribution equivalent to the case $\tau_{kl} \sim \mathcal{U}(0,0.05)$ with homogeneous coupling. Again, an increase in coupling strength resulted in a concentration of θ_k . doi:10.1371/journal.pcbi.1003736.g006

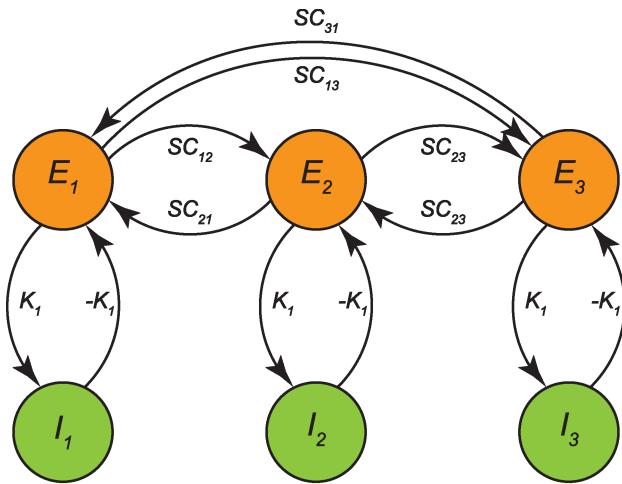


Figure 7. Neural mass coupling scheme for anatomical coupling $C_{kl}^{(inh)}$. For $C_{kl}^{(inh)}$ the SC matrix determines the coupling between excitatory units only. The SC matrix is the neuroanatomical coupling matrix; here three coupled excitatory/inhibitory pairs are shown. The other connections between excitatory and inhibitory masses serve to establish oscillatory behavior, resulting in a coupling matrix that is relatively sparse compared to $C_{kl}^{(hom)}$ and $C_{kl}^{(inh)}$. doi:10.1371/journal.pcbi.1003736.g007

although the generic solution appeared similar to the homogeneous delay case $\tau_{kl} = \tau$, it did contain $M = N$ centroid values θ_k instead of the small number $M = 2$ or $M = 4$ shown above. We depict examples of phase distributions for several parameter settings in Fig 5. Interestingly, the heterogeneity in τ_{kl} , or equivalently in Δ_{kl} , agreed with weakening the between-population coupling K_2 in that both cause a profound widening of the phase distributions; compare Fig 5A with 5C. That is, for a network with homogeneous structural connectivity, it is not the presence of delays per se that hinders synchronization but rather the distribution of delays (or the lack of coupling strength).

Inhomogeneous coupling

According to (3) both distributed phase shifts (or delays) and heterogeneous coupling may in principle result in inhomogeneity of phase coupling. In other words, distributed delays τ_{kl} and structural heterogeneity may yield inhomogeneity in functional connectivity. We therefore expected a heterogeneous coupling matrix with homogeneous delays $\tau_{kl} = \tau$ to be accompanied by desynchronization equivalent to the case of homogeneous coupling and distributed delays. To verify this, we used the inhomogeneous coupling sketched in Fig 1B, which can be given more formally as

$$C_{kl}^{(inh)} = \begin{bmatrix} C_{\mathcal{E}\mathcal{E}}^{(inh)} & C_{\mathcal{E}\mathcal{I}}^{(inh)} \\ C_{\mathcal{I}\mathcal{E}}^{(inh)} & C_{\mathcal{I}\mathcal{I}}^{(inh)} \end{bmatrix}$$

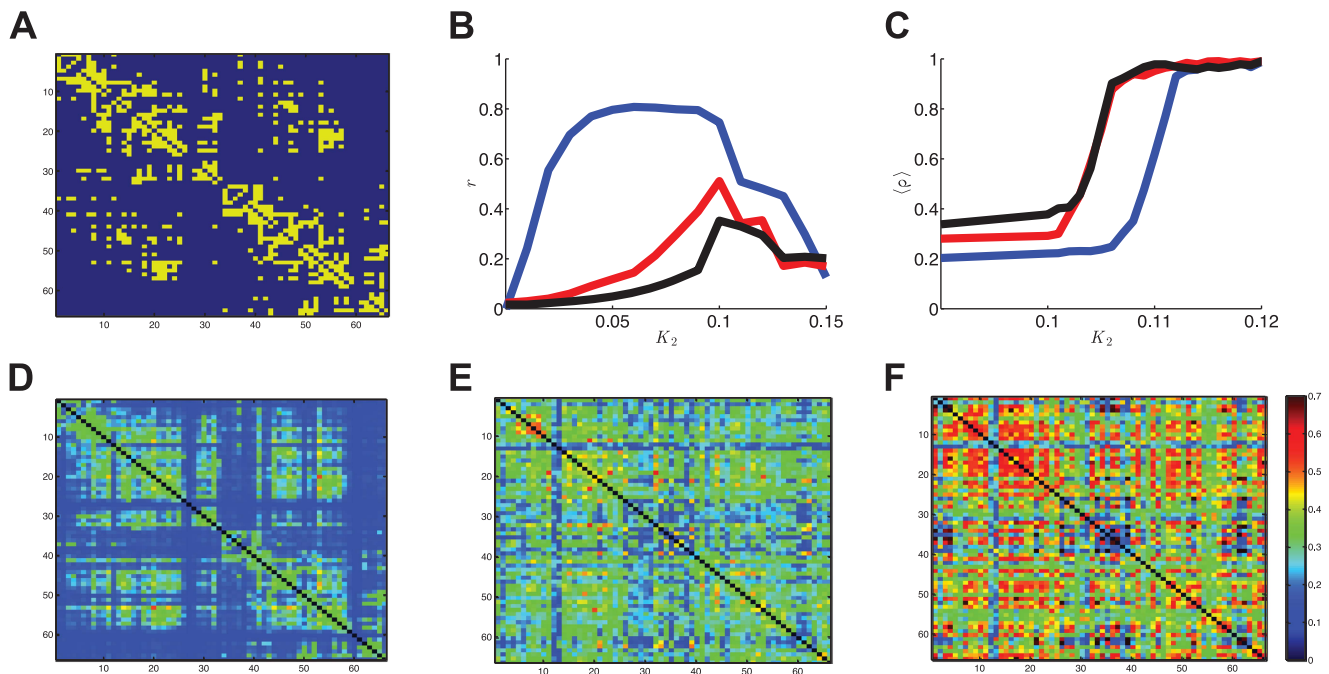


Figure 8. Anatomical connectivity matrix and resulting functional connectivities as a function of delay distribution. **A:** Sparse neuroanatomical coupling matrix $C_{\mathcal{E}\mathcal{E}}^{(N)}$ serving as structural connectivity (connections are given in yellow). **B:** Structure-function correlation $r(C_{\mathcal{E}\mathcal{E}}^{(N)}, \rho_{kl})$. **C:** Overall synchronizability $\langle \rho_{kl} \rangle$. Between-pair coupling strength K_2 appears on the horizontal axis; while blue, red, and black lines correspond to $\langle \tau_{kl} \rangle = 0, 0.05$, and 0.1 respectively. Note that an increase in delay distribution width increased synchronizability due to increased $\langle \tau_{kl} \rangle$, but the accompanying higher τ_{kl} variance decreased structure-function correspondence as predicted by (3). **D-F:** Corresponding spatial synchronization matrices ρ_{kl} for delay distributions $\tau_{kl} = 0$, $\tau_{kl} \sim \mathcal{U}(0, 0.1)$ and $\tau_{kl} \sim \mathcal{U}(0, 0.2)$ respectively ($K_2 = 0.1$). Color coding is displayed in the most right panel; only excitatory nodes are shown. doi:10.1371/journal.pcbi.1003736.g008

with sub-population connectivities

$$C_{\mathcal{E}\mathcal{E}}^{(\text{inh})} = \begin{bmatrix} 0 & & \sim\mathcal{U} \\ & \ddots & \\ \sim\mathcal{U} & & 0 \end{bmatrix} = -C_{\mathcal{I}\mathcal{I}}^{(\text{inh})}$$

$$\text{and } C_{\mathcal{I}\mathcal{E}}^{(\text{inh})} = \begin{bmatrix} K_1 & & \sim\mathcal{U} \\ & \ddots & \\ \sim\mathcal{U} & & K_1 \end{bmatrix} = -C_{\mathcal{E}\mathcal{I}}^{(\text{inh})}.$$

where $\sim\mathcal{U}$ abbreviates $\sim\mathcal{U}\left(\frac{-3K_2}{N}, \frac{5K_2}{N}\right)$ denoting that the off-(sub)diagonal entries were randomly drawn from a uniform distribution centered around $\pm \frac{K_2}{N}$.

The numerical simulations depicted in Fig 6 confirmed our hypothesis. For $C_{kl}^{(\text{inh})}$ and $\tau_{kl} = \tau = 0.05$ we observed a widening of the phase distribution similar to that shown in Figs 5B and 5C where coupling was established by $C_{kl}^{(\text{hom})}$ but with delay distributions $\tau_{kl} \sim \mathcal{U}(0, 0.2)$ and $\tau_{kl} \sim \mathcal{U}(0, 0.05)$ respectively. Increasing coupling strength reduced the width of the phase distribution comparable to the switch from Fig 5C to 5A. Functional connectivity thus seems to result from an interplay between structural connectivity C_{kl} and delay structure τ_{kl} . Therefore both should be taken into account when studying functional connectivity in neuronal networks.

Anatomical coupling

The coupling matrices C_{kl} considered so far were admittedly quite academic. However, these seminal examples did provide important insights that | as we will show here | generalize to more complicated and biologically plausible cases. We performed simulations using the coupling scheme displayed in Fig 7. The matrix $C_{kl}^{(N)}$ had the same structure as $C_{kl}^{(\text{hom})}$ but now the blocks were given by $C_{\mathcal{E}\mathcal{E}}^{(N)} = SC$, $C_{\mathcal{I}\mathcal{I}}^{(N)} = 0$, and $C_{\mathcal{I}\mathcal{E}}^{(N)} = -C_{\mathcal{E}\mathcal{I}}^{(N)} = I_{K_1}$. The acronym SC stands for ‘structural connectivity’ that here refers to a neuroanatomical connection matrix as can be derived using DTI/DSI imaging [32,33] and I_{K_1} is the identity matrix with K_1 along the diagonal. To be precise, we used a binary form of the Hagmann connection matrix; see [24] for specifics of pre-processing.

In line with earlier studies we quantified functional connectivity in terms of *phase uniformity* or *phase locking value* of the pair-wise relative phases, i.e. $\rho_{kl} = |\langle e^{i(\phi_k(t) - \phi_l(t))} \rangle|$. Using this synchronization measure, simulation results can be best summarized in the form of functional connectivity matrices constructed from ρ_{kl} values for all available pairs. The effects of delay structure τ_{kl} on these functional connectivity matrices are depicted in Figs 8D-F with the underlying structural connectivity given in Fig 8A. The functional connectivity matrix appeared rather sensitive for parameter values, as increasing coupling strength from $K_2 = 0.1$, which was the value used in Fig 8D-F, up to $K_2 = 0.12$ resulted in a fully synchronized network as can be seen in Fig 8C. The sudden synchronization is reminiscent of the phase transition towards the fully synchronized state at the critical coupling strength K_c in the Kuramoto network.

In a nutshell, from (4) we could deduce the mechanism responsible for the general finding that structural and functional connectivity are positively correlated [5,6]; see also Fig 8B. Our results clearly show that delay distribution affects both the spatial distribution of functional connectivity (Figs 8B; 8D-F) and the

overall level of synchronization in the network (Fig 8C). The increase of overall synchronization is caused by a decreased phase shift Δ_{kl} by which the phase dynamics (3) converges towards the Kuramoto model, i.e. the delay induces a change in stability of the (partially) synchronized state.

Discussion

We investigated the effect of time delays in the coupling between neural mass dynamics, where we consider an oscillatory regime, established by creating pairs of excitatory/inhibitory neural masses. Although we employed a specific neural mass model, we do consider our results generic because the mappings $C_{kl} \rightarrow D_{kl}$ and $\tau_{kl} \rightarrow \Delta_{kl}$ are largely independent of the generating nodal dynamics, presuming that the time scales in the system are sufficiently separated; cf. *Methods*.

By using this oscillatory dynamics to describe activity in certain brain areas, our approach links directly to the ongoing dispute about changes of functional connectivity in resting state networks (RSNs). There is growing evidence from experimental research that spontaneous brain activity during rest is highly structured into characteristic RSN patterns [1,3,34,35]. These activity patterns seem not to be the result of structural connectivity alone [5,36], but to reflect a non-trivial interplay between the neuroanatomical structure and dynamics [37]. The distribution of time delays involved in this dynamics may have an important role in shaping patterns of activity per se and neuronal synchronization in particular [15–17,38].

Key to our analysis was the reduction of a neural mass network to a system of phase oscillators summarized in (3). Several previous studies struggled with computational complexity when trying to unravel effects of delays vis-à-vis coupling on network dynamics [15–17,38]. By contrast, our analytic reduction ‘readily’ allowed for disentangling the contributions of both structural connectivity C_{kl} and delays τ_{kl} to the phase dynamics (3). Delays τ_{kl} entered the phase dynamics as phase shifts Δ_{kl} , given a proper time scale separation of oscillatory and phase dynamics. Furthermore, we found that heterogeneity in delays yields effects equivalent to those of heterogeneity in structural connectivity. That is, connectivity and delay effects cannot be easily distinguished when solely looking at functional connectivity patterns.

The decrease of Ω as a function of delay, as depicted in Fig 2, agreed with the analytical findings of [13] as well as with our small-delay approximations outlined in the *Methods*. However, when further comparing the current results with the literature, one has to realize that some fundamental differences exist between general phase oscillator networks and our dynamics (3). One of those differences is the finite dimensionality of the system (3). We assumed every excitatory/inhibitory neural mass pair to represent a single brain area, by which the dimension of the system under study may be fairly low. On the contrary, most analytical work on phase oscillator networks considered the limit $N \rightarrow \infty$ [14,39–41] rendering one-to-one comparisons all but trivial. This can already be appreciated by the rather dramatic finite-size effects in Kuramoto networks [42–45]. Moreover, our structural connectivity $C_{kl}^{(\text{hom})}$ is rather atypical due to its strong \pm -asymmetry. Usually, the connectivity structure in similar phase oscillator networks comprises either fully homogeneous coupling or the entries C_{kl} are distributed according to some unimodal distribution [42,46]. An exception is [47], who investigated repulsive coupling, which is similar to the excitatory/inhibitory connections in $C_{kl}^{(\text{hom})}$. That study reported the presence of two anti-phase clusters reminiscent of the separate \mathcal{E}/\mathcal{I} -groups observed here.

The time scale separation in (3) and the resulting simplification of delays τ_{kl} as phase shifts Δ_{kl} also hinders direct comparison with studies on delays in the Kuramoto network. This may indeed explain our seemingly contradicting results. For example, we did not observe the emergence of multi-stability mediated by specific (τ, K) -combinations as reported in [12,48]. In those studies, regions in the (τ, K) phase plane were found in which synchronization was entirely absent. This is clearly not the case in our study. We did find synchronized solutions irrespective of delays. This is not trivial, because for $\tau_{kl} = 0$ the phase dynamics equation (3) may be reduced to a cosine-variant of the traditional Kuramoto model, which is known for its inability to display synchronized behavior [49]. By exploiting the pairing of the \mathcal{E}/\mathcal{I} -groups and the \pm -asymmetry in $C_{kl}^{(hom)}$ we could map our averaged neural mass network to a conventional, fully homogeneous Kuramoto network via a mere transformation of variables. Hence our system can display synchronized behavior even for vanishing τ values. This is consistent with [50] who did not find any qualitative effects of a phase shift α on the stability of the Kuramoto network.

Apart from choosing random values as entries of the C_{kl} -matrix, inhomogeneous coupling might also stem from creating distinctively different sub-populations in the network. It can then be studied by modifying within- versus between-network interactions. Particularly interesting in this respect is the occurrence of clustering in the network. When delays are not incorporated one needs either structural inhomogeneity [51] or higher-order Fourier harmonics, in combination with an appropriate phase shift [30], to achieve clustering. The phenomenon of clustering is important in the light of the study of RSNs, i.e. the strong spatiotemporal organization observed in brain activity during resting state conditions [1,3,34,35].

We briefly consider a simple, low-dimensional example of three isolated excitatory nodes. We define a cluster as a number of (excitatory) masses attaining the same centroid phase value θ_k . By denoting the excitatory and inhibitory centroid values as $\theta_{\mathcal{E}}$ and $\theta_{\mathcal{I}}$, respectively and assuming $\tau_{k,k+N/2} = 0$, from the phase derivation (3) and its corresponding continuity equation (4) one finds constraining equations

$$\omega + \alpha\beta K_1 \sin\left(\theta_{\mathcal{I}} - \theta_{\mathcal{E}} + \frac{\pi}{2}\right) = \begin{cases} \alpha\beta \frac{R_{\mathcal{I}}}{R_{\mathcal{E}}} (D_{12} \sin \Delta_{12} + D_{13} \sin \Delta_{13}) \\ \alpha\beta \frac{R_{\mathcal{I}}}{R_{\mathcal{E}}} (D_{21} \sin \Delta_{21} + D_{23} \sin \Delta_{23}) \\ \alpha\beta \frac{R_{\mathcal{I}}}{R_{\mathcal{E}}} (D_{31} \sin \Delta_{31} + D_{32} \sin \Delta_{32}) \end{cases}$$

for $0 \leq \Omega\tau \leq \frac{\pi}{2}$. In fact, these forms already hint at the interference between coupling and delays and its effect on synchronization structure. First, all terms on the right-hand side must have equal magnitude requiring specific combinations of D_{kl} and Δ_{kl} . However, both D_{kl} and Δ_{kl} are constrained by biology: D_{kl} by the neuroanatomical coupling SC as part of C_{kl} ; and Δ_{kl} by the spatial structure of the brain, as delays are proportional to distance between masses k and l due to finite conduction velocity. Second, because the left-hand side does not vanish, D_{kl} must have some lower bound. If $C_{kl} \ll 1$, then $\sin \Delta_{kl}$ cannot compensate this and the equality cannot be satisfied. Because C_{kl} determines D_{kl} , there must be some minimal coupling strength between nodes for synchronization to emerge. This explains the positive correlation

between structural and functional connectivity, see, e.g., [6,17,38]. It also shows the intricate interplay between structure and delays in establishing synchronization structure.

Interestingly, D_{kl} may be regarded as the effective coupling matrix that is typically encountered in dynamic causal modeling approaches [52]. The fact that D_{kl} is directly determined by C_{kl} also explains the finding that models using the structural connectivity as a prior do show more evidence than models using other priors [53]. That is, models that have structural connectivity as a starting point, perform better in terms of data explanation. The sparsity of D_{kl} induced by C_{kl} may yield coexisting synchronized and desynchronized groups within the network, which are often labelled chimera states in the study of phase oscillator systems. It has been found that they crucially depend on the combination of coupling strengths and phase shifts [45,54,55] (or delays [56]), confirming that there has to be a specific matching of coupling and delays for synchronization to occur.

Against the background of the aforementioned τ_{kl} -dependence of functional connectivity and the functional-structural connectivity correlation for a biological plausible network, we numerically investigated this by performing simulations of (1) with structural connectivity given by the anatomical connectivity matrix $C_{kl}^{(N)}$ reported by Hagmann and co-workers [32]. Functional connectivity was quantified as pair-wise phase uniformity, i.e. the phase locking value. Our numerical assessment is summarized in Fig 8. It clearly revealed off-diagonal patches with synchronization between nodes that are not coupled (contradicting what has been sketched above). The topology of the Hagmann et al. network shares similarities with the Watts and Strogatz' small-world network [57], i.e. both have a relatively large clustering coefficient with a small average path length. This kind of topology is often believed to be generic in biological neural networks like our brain [5] and enhances synchronizability compared to random networks [57–59]. The presence of sparsely connected clusters establishes synchronization between nodes that are only indirectly coupled via their clusters. This causes ‘blurring’ of the structural connectivity matrix: The functional connectivity matrix is less sparse than the structural one [60]. Although this ‘blurring’ is similar to the effects attributed to volume conduction [61], in this case it is solely due to network topology.

Next to such clustering phenomena, we can make even more general predictions about the effect of delays in this network. Structural and functional connectivity are most prominently correlated for homogeneous delays, since $\Delta_{kl} = \Delta$ yields an interaction term in (3) that is merely a scaled version of $C_{kl}^{(N)}$. Hence, the resulting spatial synchronization distribution largely resembles D_{kl} and thus $C_{kl}^{(N)}$, presuming that the overall coupling strength is not excessively large. This effect can be seen in Fig 8B, where we depicted the Pearson correlation coefficient between the lower triangular parts of $C_{\mathcal{E}\mathcal{E}}^{(N)}$ and the functional connectivity matrix ρ_{kl} . Increasing the width of the delay distribution results in a decrease in structure-function correspondence. The positive correlations are consistent with the finding that the pattern of resting state activity is spanned by the eigenmodes of the underlying connectivity matrix in [62]. This is not as trivial as it may seem because the node dynamics in this study were noise-driven fluctuations around a stable fixed point and therefore entirely different from the self-sustained oscillations considered in the current study.

Widening the delay distribution also had another effect: It increased its average value and consequently the mean phase shift $\langle \Delta_{kl} \rangle = \langle \frac{\pi}{2} - \Omega\tau_{kl} \rangle$ tended to vanish. Therefore, the interaction

term $D_{kl} \sin(\phi_l - \phi_k + \Delta_{kl})$ became more similar to an ‘ordinary’ sine-term, which is known for its capacity to enhance synchronizability [63]. We illustrate this effect in Fig 8C, where overall synchrony $\langle \rho \rangle$ is shown as a function of coupling strength K_2 for different average delay-values $\langle \tau_{kl} \rangle$. A similar phenomenon has been reported for a system of coupled Hindmarsh-Rose neurons, where a stable synchronized region appears to exist despite the presence of a (constant) delay [64].

Throughout this study we assumed the amplitudes to be constant. The relation between the envelope dynamics of M/EEG and fMRI-BOLD signals [3] suggests that considering the temporal change of the amplitude may be very important for unravelling the spatio-temporal structure of resting state brain activity. Given that we focused on phase synchronization together with the slow time scale on which the BOLD dynamics evolve (<0.1 Hz, [1]), we believe that the assumption of constant amplitude is justified here. Investigating this assumption in depth, however, is beyond the scope of the current study.

We summarize that the dynamics of a system of coupled Freeman neural masses (1) can be captured by the averaged phase dynamics (3), in which the role of the structural connectivity C_{kl} and delay distribution τ_{kl} become explicit. By this, one can identify the relative contributions of structure and delay to phase synchronization, i.e. to the functional connectivity of the neural network. Heterogeneity in structural coupling and distributed delays have equivalent effects on the observed phase distributions. Overall, this supports the notion that structure and delay are both crucial determinants of network behavior and should therefore be taken into account in unison whenever modeling realistic neural networks [37]. Our examples on clustering detailed how the intricate interplay between coupling and delays determines the form and spatial distribution of clustering in these networks. Pinpointing the explicit contributions of τ_{kl} and C_{kl} in the phase dynamics (3) enabled us to understand their roles in establishing synchronization structure and why functional and structural connectivity are so closely correlated. This implies that the observed temporal changes in synchronization structure in resting state and task conditions can be modulated through either τ_{kl} or amplitudes R_k .

Methods

To analyze the gross membrane voltage of a neural mass we first wrote its dynamics (1) as a two-dimensional system using the auxiliary variable $U_k = \dot{V}_k$. For the sake of simplicity we further rewrote the convolution integral in (1) by means of $[W(t) * S[V_l(t - \tau_{kl})]] = [W(t - \tau_{kl}) * S[V_l(t)]]$. Then the dynamics (1) reads

$$\begin{aligned} \dot{V}_k &= U_k \\ \dot{U}_k &= -(\alpha_k + \beta_k)U_k - \alpha_k \beta_k V_k + \alpha_k \beta_k q_k \\ &\quad + \alpha_k \beta_k \sum_{l=1}^N C_{kl} [W(t - \tau_{kl}) * S[V_l(t)]]. \end{aligned} \quad (6)$$

In the following we discuss this dynamics in its oscillatory regime after transforming the system into polar coordinates to derive the corresponding phase dynamics. That transform, however, was not applied to the original state variables $[V_k, U_k]$ but to the deviations $[\delta V_k, \delta U_k]$ around the unstable fixed points

$[V_k^{(0)}, U_k^{(0)}]$, i.e. we transformed $[V_k, U_k] \rightarrow [V_k^{(0)} + \delta V_k, U_k^{(0)} + \delta U_k]$. Furthermore, we expanded $S[V_k(t)]$ around $V_k^{(0)}$ in the sense of Taylor and obtained

$$S[V_k^{(0)} + \delta V_k(t)] = \sum_{n=0}^{\infty} \frac{1}{n!} S^{(n)}[V_k^{(0)}] (\delta V_k)^n. \quad (7)$$

With this expansion the dynamics of the deviations $\delta V_k, \delta U_k$ could be approximated as

$$\begin{aligned} \dot{\delta V}_k &= \delta U_k \\ \dot{\delta U}_k &\approx -(\alpha_k + \beta_k)\delta U_k - \alpha_k \beta_k \delta V_k \\ &\quad + \alpha_k \beta_k \sum_{l=1}^N C_{kl} [W(t - \tau_{kl}) * S'[V_l^{(0)}] \delta V_l(t)]. \end{aligned} \quad (8)$$

A closer look at this linear system revealed that the fixed points $[V_k^{(0)}, U_k^{(0)}]$ were indeed unstable nodes, provided that a proper balance between excitatory and inhibitory masses was present. That is, the eigenvalues of the linear system (8) were complex-valued with positive real-parts — explicit expressions for the eigenvalues (as a function of delay) can be found below.

Next, we transformed system (8) into polar coordinates by means of $[\delta V_k, \delta U_k] \rightarrow [R_k \cos(\Omega t + \phi_k), -\Omega R_k \sin(\Omega t + \phi_k)]$ so that the phases could be cast into the generic dynamics

$$\dot{\phi}_k = -\Omega + \frac{1}{\Omega R_k^2} (\delta U_k \dot{V}_k - \delta V_k \dot{U}_k). \quad (9)$$

Importantly, in the current case we could assume that the phase dynamics (9) in general contains two (or more) distinct time scales: the rate of change given by the oscillation defined via the frequency Ω and the time scale(s) of the amplitudes R_k and the phases ϕ_k ; the latter are much slower than $2\pi/\Omega$ and can hence be separated. More formally we used

$$|\dot{R}_k/R_k| \ll \Omega \quad \text{and} \quad |\dot{\phi}_k/\phi_k| \ll \Omega.$$

In first order approximation we could thus consider R_k and ϕ_k to be constant during one period of oscillation, $T = 2\pi/\Omega$. This approach is referred to as a combination of a *rotating wave approximation* and a *slowly varying amplitude approximation* [65]. It enabled us to average the dynamics over the interval $[0, T]$; see also [23]. As will be shown in the following, this averaging procedure decoupled amplitude and phase dynamics, which ultimately resulted in the dynamics (3). Below we will provide a more formal discussion regarding these approximations.

Averaging—towards the phase oscillator model

To average the dynamics (9) we defined the averaging operator as $\langle f(s) \rangle = \int_0^T f(s) ds$. We first substituted (8) into (9) and used

$$\langle \delta V_k \delta U_k \rangle = 0, \quad \langle \delta V_k^2 \rangle = \frac{R_k^2}{2}, \quad \text{and} \quad \langle \delta U_k^2 \rangle = \frac{\Omega^2 R_k^2}{2}.$$

The convolution integral on the right-hand side of the second equation of (8) required more attention. Recall the definition of W in (2) and the definition of the convolution operator, with which one can write

$$\begin{aligned}
 [W(t-\tau_{kl}) * \delta V_l(t)] &= \int_{-\infty}^{\infty} W(t-\tau_{kl}-s) \delta V_l(s) ds \\
 &= \int_{-\infty}^{\infty} \gamma e^{-\gamma(t-\tau_{kl}-s)} R_l \cos(\Omega s + \phi_l) ds \\
 &= R_l \gamma e^{-\gamma(t-\tau_{kl})} \int_{-\infty}^{t-\tau_{kl}} e^{\gamma s} \cos(\Omega s + \phi_l) ds \\
 &= \frac{\gamma R_l}{\gamma^2 + \Omega^2} \{ \gamma \cos(\Omega(t-\tau_{kl}) + \phi_l) + \Omega \sin(\Omega(t-\tau_{kl}) + \phi_l) \}. \quad (10)
 \end{aligned}$$

When multiplied by $\delta V_k(t)$, this yielded the two averaged trigonometric expressions

$$\begin{aligned}
 \langle R_k \cos(\Omega t + \phi_k) \frac{R_l \gamma^2}{\gamma^2 + \Omega^2} \cos(\Omega(t-\tau_{kl}) + \phi_l) \rangle \\
 = \frac{1}{2} \frac{\gamma^2 R_l R_k}{\gamma^2 + \Omega^2} \{ \cos(\Omega \tau_{kl}) \cos(\phi_l - \phi_k) + \sin(\Omega \tau_{kl}) \sin(\phi_l - \phi_k) \}
 \end{aligned}$$

and

$$\begin{aligned}
 \langle R_k \cos(\Omega t + \phi_k) \frac{\Omega \gamma R_l}{\gamma^2 + \Omega^2} \sin(\Omega(t-\tau_{kl}) + \phi_l) \rangle \\
 = \frac{1}{2} \frac{\Omega \gamma R_l R_k}{\gamma^2 + \Omega^2} \{ \cos(\Omega \tau_{kl}) \sin(\phi_l - \phi_k) - \sin(\Omega \tau_{kl}) \cos(\phi_l - \phi_k) \}.
 \end{aligned}$$

After substituting this in (9) we obtained the phase dynamics

$$\begin{aligned}
 \dot{\phi}_k &= \omega_k - \alpha_k \beta_k \sum_{l=1}^N A_{kl} \sin(\phi_l - \phi_k) - \\
 &\quad \alpha_k \beta_k \sum_{l=1}^N B_{kl} \cos(\phi_l - \phi_k) \quad (11)
 \end{aligned}$$

where we defined the constants A_{kl} and B_{kl} as

$$\begin{aligned}
 A_{kl} &= \frac{\gamma^2 \sin(\Omega \tau_{kl}) + \Omega \gamma \cos(\Omega \tau_{kl})}{2\Omega(\gamma^2 + \Omega^2)} \frac{R_l}{R_k} S' [V_l^{(0)}] C_{kl} \\
 B_{kl} &= \frac{\gamma^2 \cos(\Omega \tau_{kl}) - \Omega \gamma \sin(\Omega \tau_{kl})}{2\Omega(\gamma^2 + \Omega^2)} \frac{R_l}{R_k} S' [V_l^{(0)}] C_{kl}.
 \end{aligned}$$

By this procedure we omitted all fast oscillating terms as they averaged out (cf. *rotating wave approximation*).

As mentioned in the *Results* section, we focused on the case in which our convolution kernel W did not contain any memory. That is, we considered the limit $\gamma \rightarrow \infty$. In this limit only the first terms in the numerators of A_{kl} and B_{kl} remained non-zero and we could cast (11) in the form (3) using

$$D_{kl} = \sqrt{A_{kl}^2 + B_{kl}^2} = \frac{1}{2\Omega} \frac{R_l}{R_k} S' [V_l^{(0)}] C_{kl} \quad \text{and} \quad \Delta_{kl} = \frac{\pi}{2} - \Omega \tau_{kl}.$$

Note that in this form, the delays τ_{kl} only appeared in the phase shift Δ_{kl} . Last but not least we simplified expression (3) by exploiting the homogeneity of $C_{kl}^{(\text{hom})}$ to explicitly formulate the

D_{kl} matrix multiplication. In particular for equal delays, i.e. for $\tau_{kl} = \tau$, this led to a greatly simplified form of (4) that we summarized in the *Results* section and will be discussed in more detailed below.

Fixed points and amplitudes

The neural masses do not oscillate around the origin but around the fixed points $[V_k^{(0)}, U_k^{(0)}]$, which have a direct influence on the coupling terms D_{kl} through the term $S' [V_l^{(0)}]$. Delay values τ_{kl} do not influence the positions of the fixed points $[V_k^{(0)}, U_k^{(0)}]$ because by definition $[\dot{V}_k^{(0)}, \dot{U}_k^{(0)}] = [0, 0]$. Hence, $V_k(t - \tau_{kl}) = V_k(t)$ holds, presuming the fixed points exist. Therefore we were free to choose $\tau_{kl} = 0$, such that under the limit $\gamma \rightarrow \infty$ the coupling term in (6) reduced to

$$\alpha_k \beta_k \sum_{l=1}^N C_{kl} \int_{-\infty}^{\infty} W(t - \tau_{kl} - s) S [V_l^{(0)}] ds \rightarrow \alpha_k \beta_k \sum_{l=1}^N C_{kl} S [V_l^{(0)}].$$

After inserting the form of $C_{kl}^{(\text{hom})}$ we explicitly found

$$V_k^{(0)} = \begin{cases} \frac{2K_{\mathcal{E}}}{N} \sum_{l \in \mathcal{E}} S [V_l^{(0)}] - \frac{2K_{\mathcal{I}}}{N} \sum_{l \neq k + N/2} S [V_l^{(0)}] - K_{\mathcal{I}} S [V_{k+N/2}^{(0)}] + q_k & \text{for } k \in \mathcal{E} \\ \frac{2K_{\mathcal{I}}}{N} \sum_{l \neq k - N/2} S [V_l^{(0)}] - \frac{2K_{\mathcal{E}}}{N} \sum_{l \in \mathcal{E}} S [V_l^{(0)}] + K_{\mathcal{E}} S [V_{k-N/2}^{(0)}] + q_k & \text{for } k \in \mathcal{I} \end{cases},$$

which implied $V_k^{(0)} = V_{\mathcal{E}}^{(0)}$, $\forall k \in \mathcal{E}$ and $V_k^{(0)} = V_{\mathcal{I}}^{(0)}$, $\forall k \in \mathcal{I}$. That is, in the case of the homogeneous coupling the fixed points of the excitatory masses are equal and the same holds for the inhibitory masses.

The coupling D_{kl} also depended on the amplitudes R_k of the neural masses — see also [24]. Accounting for the high degree of homogeneity in the system, we assumed the amplitudes to be equal for equal types of neural masses, i.e. $R_k = R_{\mathcal{E}}$, $k \in \mathcal{E}$ and $R_k = R_{\mathcal{I}}$, $k \in \mathcal{I}$. Furthermore we randomized the parameters $\alpha_k = \alpha + \varepsilon$, $\beta_k = \beta + \varepsilon$ by introducing ε as a mean-centered random variable. Whenever appropriate we chose ε sufficiently small to restrict discussion to the mean values $\alpha = 1/N \sum_{k=1}^N \alpha_k$ and $\beta = 1/N \sum_{k=1}^N \beta_k$.

Homogeneous coupling — existence of solutions

Since the phase oscillator system (3) can be cast in Kuramoto form, fully synchronized solutions may be stable despite the presence of equal delays $\tau_{kl} = \tau$. But how about solutions other than the fully synchronized ones? In what follows we discuss existence and form of partially synchronized solutions of (3) for general delays τ_{kl} . We concentrated on homogeneous coupling and varied the distribution of τ_{kl} . In the homogeneous case we found the dynamics of the k -th node's phase distribution \mathcal{P}_k to be

$$\begin{aligned}
 \frac{\partial}{\partial t} \mathcal{P}_k(\phi_k, t) &= - \frac{\partial}{\partial \phi_k} \left[\Omega - \Gamma_{\mathcal{E}} \int_0^{2\pi} \sum_{l \in \mathcal{E}} \sin(\tilde{\phi}_l - \phi_k + \Delta_{kl}) \mathcal{P}_l(\tilde{\phi}_l, t) d\tilde{\phi}_l \right. \\
 &\quad \left. + \Gamma_{\mathcal{I}} \int_0^{2\pi} \sum_{l \in \mathcal{I}} \sin(\tilde{\phi}_l - \phi_k + \Delta_{kl}) \mathcal{P}_l(\tilde{\phi}_l, t) d\tilde{\phi}_l \right] \mathcal{P}_k(\phi_k, t) \quad (12)
 \end{aligned}$$

where the subscript $\circ = \mathcal{E}$ when $k \in \mathcal{E}$ and $\circ = \mathcal{I}$ when $k \in \mathcal{I}$. Note

that equation (12) may differ for every k . Homogeneity of $C_{kl}^{(\text{hom})}$ enable us to express D_{kl} explicitly and to define the following constants

$$\begin{aligned}\Gamma_{\mathcal{E}\mathcal{E}} &= \alpha\beta K_2 \frac{N-2}{N} S' [V_{\mathcal{E}}^{(0)}], \\ \Gamma_{\mathcal{E}\mathcal{I}} &= \alpha\beta \frac{R_{\mathcal{I}}}{R_{\mathcal{E}}} \left[K_1 S' [V_{\mathcal{I}}^{(0)}] + K_2 \frac{N-2}{N} S' [V_{\mathcal{I}}^{(0)}] \right] \\ \Gamma_{\mathcal{I}\mathcal{E}} &= \alpha\beta \frac{R_{\mathcal{E}}}{R_{\mathcal{I}}} \left[K_1 S' [V_{\mathcal{E}}^{(0)}] + K_2 \frac{N-2}{N} S' [V_{\mathcal{E}}^{(0)}] \right], \\ \Gamma_{\mathcal{I}\mathcal{I}} &= \alpha\beta K_2 \frac{N-2}{N} S' [V_{\mathcal{I}}^{(0)}].\end{aligned}\quad (13)$$

Sufficient for the existence of a stationary solution is the case in which the drift coefficient in the dynamics of the probability density vanishes, here the bracketed term on the right-hand side of (12). From the dynamics (12) it readily follows that the phase distribution obeys the form (5), i.e. $\mathcal{P} = \mathcal{P}_{\text{stat}}(\phi_1, \dots, \phi_N)$, containing N different centroid phase values θ_k .

Equal delays. $\tau_{kl} = \tau$. As said, for homogeneous coupling the sums in (12) could be evaluated in the form of the constants in (13). Furthermore in the case of equal delays $\tau_{kl} = \tau$ (i.e. $\Delta_{kl} = \Delta$) we only had to account for two distinct populations each with just a single type of density dynamics, by which the system (12) of N equations could be reduced to merely two distinct ones:

$$\begin{aligned}\frac{\partial}{\partial t} \mathcal{P}_{\mathcal{E}}(\phi_{\mathcal{E}}, t) &= -\frac{\partial}{\partial \phi_{\mathcal{E}}} \left[\omega - \Gamma_{\mathcal{E}\mathcal{E}} \int_0^{2\pi} \sin(\tilde{\phi}_{\mathcal{E}} - \phi_{\mathcal{E}} + \Delta) \mathcal{P}_{\mathcal{E}}(\tilde{\phi}_{\mathcal{E}}, t) d\tilde{\phi}_{\mathcal{E}} \right. \\ &\quad \left. + \Gamma_{\mathcal{E}\mathcal{I}} \int_0^{2\pi} \sin(\tilde{\phi}_{\mathcal{I}} - \phi_{\mathcal{E}} + \Delta) \mathcal{P}_{\mathcal{I}}(\tilde{\phi}_{\mathcal{I}}, t) d\tilde{\phi}_{\mathcal{I}} \right] \mathcal{P}_{\mathcal{E}}(\phi_{\mathcal{E}}, t) \\ \frac{\partial}{\partial t} \mathcal{P}_{\mathcal{I}}(\phi_{\mathcal{I}}, t) &= -\frac{\partial}{\partial \phi_{\mathcal{I}}} \left[\omega - \Gamma_{\mathcal{I}\mathcal{E}} \int_0^{2\pi} \sin(\tilde{\phi}_{\mathcal{E}} - \phi_{\mathcal{I}} + \Delta) \mathcal{P}_{\mathcal{E}}(\tilde{\phi}_{\mathcal{E}}, t) d\tilde{\phi}_{\mathcal{E}} \right. \\ &\quad \left. + \Gamma_{\mathcal{I}\mathcal{I}} \int_0^{2\pi} \sin(\tilde{\phi}_{\mathcal{I}} - \phi_{\mathcal{I}} + \Delta) \mathcal{P}_{\mathcal{I}}(\tilde{\phi}_{\mathcal{I}}, t) d\tilde{\phi}_{\mathcal{I}} \right] \mathcal{P}_{\mathcal{I}}(\phi_{\mathcal{I}}, t).\end{aligned}\quad (14)$$

To show the existence of $\mathcal{P}_{\text{stat},2}(\phi_{\mathcal{E}}, \phi_{\mathcal{I}})$ consisting of two phase clusters, one for the excitatory units and one for the inhibitory units, i.e.

$$\mathcal{P}_{\text{stat},2}(\phi_{\mathcal{E}}, \phi_{\mathcal{I}}) = \frac{1}{2} \delta(\phi_{\mathcal{E}} - \theta_{\mathcal{E}}) + \frac{1}{2} \delta(\phi_{\mathcal{I}} - \theta_{\mathcal{I}})$$

we followed a constructive approach and substituted $\mathcal{P}_{\text{stat},2}(\phi_{\mathcal{E}}, \phi_{\mathcal{I}})$ into (14). Vanishing of the drift coefficient required

$$(\Gamma_{\mathcal{E}\mathcal{E}} + \Gamma_{\mathcal{I}\mathcal{I}}) \sin \Delta = \Gamma_{\mathcal{E}\mathcal{I}} \sin(\Delta + \psi) + \Gamma_{\mathcal{I}\mathcal{E}} \sin(\Delta - \psi). \quad (15)$$

when abbreviating $\psi = \theta_{\mathcal{E}} - \theta_{\mathcal{I}}$. Using $|\Gamma_{\mathcal{I}\mathcal{E}} + \Gamma_{\mathcal{E}\mathcal{I}}| > |\Gamma_{\mathcal{E}\mathcal{E}} + \Gamma_{\mathcal{I}\mathcal{I}}|$, which followed from (13) irrespective of the value of K_2 , we could conclude that a solution ψ satisfying (15) exists. Note that only ψ appeared in (15) and not the centroid values θ_k , which allows for the mapping to the conventional Kuramoto model as will be discussed below.

We could readily generalize this line of reasoning to an arbitrary number of clusters after defining the stationary phase probability density containing M clusters as

$$\mathcal{P}_{\text{stat},M}(\phi_1, \dots, \phi_M) = \frac{1}{M} \sum_{k=1}^{M/2} \delta(\phi_{\mathcal{E}} - \theta_{\mathcal{E},k}) + \frac{1}{M} \sum_{k=M/2+1}^M \delta(\phi_{\mathcal{I}} - \theta_{\mathcal{I},k}).$$

We defined generalized phase differences $\psi_{ab,kl} = \theta_{a,k} - \theta_{b,l}$ where $a, b \in \{\mathcal{E}, \mathcal{I}\}$ and $k, l \in \{1, \dots, M\}$, by which we obtained the set of constraining equations as

$$\begin{aligned}\Gamma_{\mathcal{E}\mathcal{E}} \left[\sum_{l \in \mathcal{E}} \sin(\psi_{\mathcal{E}\mathcal{E},lk} + \Delta_{kl}) \right] &+ \Gamma_{\mathcal{I}\mathcal{I}} \left[\sum_{l \in \mathcal{I}} \sin(\psi_{\mathcal{I}\mathcal{I},lk} + \Delta_{kl}) \right] \\ &= \Gamma_{\mathcal{E}\mathcal{I}} \left[\sum_{l \in \mathcal{I}} \sin(\psi_{\mathcal{I}\mathcal{E},lk} + \Delta_{kl}) \right] \\ &+ \Gamma_{\mathcal{I}\mathcal{E}} \left[\sum_{l \in \mathcal{E}} \sin(\psi_{\mathcal{E}\mathcal{I},lk} + \Delta_{kl}) \right].\end{aligned}\quad (16)$$

In contrast to (15) we here considered general delays τ_{kl} , but note that the form of (16) did not change for $\tau_{kl} = \tau$. As the values of the constants Γ still fulfilled the inequality $|\Gamma_{\mathcal{I}\mathcal{E}} + \Gamma_{\mathcal{E}\mathcal{I}}| > |\Gamma_{\mathcal{E}\mathcal{E}} + \Gamma_{\mathcal{I}\mathcal{I}}|$ we again could conclude that this system can be solved. Thus, even for equal delays $\tau_{kl} = \tau$ (or $\Delta_{kl} = \Delta$) the stationary phase distribution may contain any number of clusters $M \leq N$. Of course, this existence proof does not imply that all these solutions will be found in reality since we have not yet addressed their stability; cf. Figs 4A and 3A. Note that apart from the fully synchronized state, we here restricted our stability analysis to numerical evaluations.

The distributed delay case (16) does not require $\Delta_{kl} = \Delta$. Hence, for general Δ_{kl} the stationary distribution $\mathcal{P}_{\text{stat},M}$ will contain $M = N$ centroid values θ_k with $k \in \{1, \dots, M\}$.

Stability for $\tau_{kl} = \tau$ — a fling with the Kuramoto network. Before proving the existence of distinct solutions in the case of arbitrary delays τ_{kl} , we first briefly discuss the case of constant delay because it readily links the model (3) to the Kuramoto network of coupled phase oscillators [63]. For $\tau_{kl} = \tau = 0$, the interaction term in (3) reduces to a mere cosine term because of $\Delta_{kl} = \frac{\pi}{2}$. We note that in Kuramoto's traditional form this cosine term leads to a system that is unable to show synchronized solutions [49]. Our numerical simulations, however, revealed synchronized solutions; see, e.g., Figs 3 and 4. In what follows we show that due to the fact that the centroid phase values θ_k are irrelevant one can distill the traditional Kuramoto model.

It is the coupling matrix $C_{kl}^{(\text{hom})}$ that made the difference with Kuramoto's network as we assumed a (balanced) combination of excitatory and inhibitory units. In the given form illustrated in Fig 1A, the matrix $C_{kl}^{(\text{hom})}$ is strictly speaking not homogeneous but contains an asymmetry. This, however, did allow for mapping our model to the Kuramoto network by adapting an approach of Frank and co-workers [31]. In essence, we applied a change in variables yielding a fully homogeneous coupling matrix. For the sake of legibility we set $R_{\mathcal{E}} = R_{\mathcal{I}}$, $S' [V_{\mathcal{I}}^{(0)}] = S' [V_{\mathcal{E}}^{(0)}]$ and $K_1 = 2K_2$.

Then D_{kl} simplified to $D_{kl} = \pm \frac{\alpha\beta K_2}{\Omega N} S' [V^{(0)}]$ where the ' \pm '-sign discriminates rows that correspond to the excitatory/inhibitory neural masses \mathcal{E}/\mathcal{I} , respectively. By this simplification the key feature of the system (9), the asymmetry in the coupling matrix, remained untouched.

We further transformed the system into a rotating frame at frequency $\omega = \frac{\alpha\beta - \Omega^2}{2\Omega}$ by defining [65,66]

$$\varphi_k = \begin{cases} \phi_k - \omega t, & k \in \mathcal{E} \\ \phi_k - \pi - \omega t & k \in \mathcal{I} \end{cases} \quad (17)$$

After abbreviating the constants $\frac{\alpha\beta}{\Omega} K_2 S' [V^{(0)}] = \kappa$, the phase dynamics (9) became

$$\dot{\varphi}_k = -\frac{\kappa}{N} \sum_{l=1}^N \sin(\varphi_l - \varphi_k + \Delta).$$

In line with Kuramoto's analysis we introduced a mean (or cluster) phase θ and amplitude ρ in terms of $\rho e^{i\theta} = \frac{1}{N} \sum_{l=1}^N e^{i(\varphi_l + \Delta)}$ that represent well-known order parameter(s). Finally, substituting

$$\frac{1}{N} \sum_{l=1}^N \sin(\varphi_l - \varphi_k + \Delta) = \rho \sin(\theta - \varphi)$$

$$\dot{\varphi} = -\kappa\rho \sin(\vartheta - \varphi).$$

Here we dropped the subscript k because the equation applies for all nodes. This dynamics agrees entirely with the Kuramoto model, apart from the fact that we here considered $\alpha_k = \alpha$ and $\beta_k = \beta$ by which all oscillators' natural frequencies $\omega_k = \omega$ agree. Due to this correspondence to the Kuramoto model, we could conclude that the system with equal delays $\tau_{kl} = \tau$ and 'homogeneous' coupling matrix $C_{kl}^{(hom)}$ can generate synchronized states provided the overall coupling strength $\frac{\alpha\beta}{\Omega} K_2 S' [V^{(0)}]$ is properly chosen.

Numerical assessments

Both distributed delays τ_{kl} and heterogeneous coupling called for numerical assessments, particularly when it came to the stability of solutions. We performed numerical simulations of the coupled neural masses (1) using a conventional Euler-forward integration scheme with time step $\Delta t = 10^{-3} s$ over a time span of 10 s. We verified the appropriateness of this simple implementation against a more elaborate predictor/corrector integrator [67], which revealed little to no difference but demanded far more numerical resources. The simulated network consisted of 500 nodes (250 \mathcal{E}/\mathcal{I} pairs) with α_k and β_k being randomly drawn from uniform distributions ($\alpha_k \in [25,75]$ and $\beta_k \in [175,225]$) to mimic distributed natural frequencies per \mathcal{E}/\mathcal{I} -pair of nodes. Although randomly drawn, these sets were fixed across simulations trials. Initial conditions were chosen randomly and did vary between trials; $V_k(t=0) \in [-100,100], k \in \mathcal{E}, V_k(t=0) \in [-10,60], k \in \mathcal{I}$ and similarly for $\dot{V}_k(t=0)$. The external input q_k was set to $q_k = 20, k \in \mathcal{E}, q_k = 0, k \in \mathcal{I}$. Coupling between masses was achieved by using the sigmoidal activation function $S[V]$ that was given as

$$S[V] = \gamma \frac{1}{1 + e^{-(V - V_{th})/\sigma}}.$$

The fraction in this equation may be interpreted as the cumulative distribution function of the normal distribution $\mathcal{N}(V - V_{th}, \sigma^2)$ of the firing thresholds V_{th} across the population,

whereas the constant γ is just a scaling factor [68]. In the simulations we used the following values for the activation function parameters: $\gamma = 250, V_{th} = 15$ and $\sigma = 1$.

In order to compare the numerics with our analytical results, we determined the phase values ϕ_k from the simulated potentials $V_k(t)$ by means of the Hilbert phase. To this end, we first determined oscillation frequency Ω as the lowest frequency with a coinciding peak in the power spectra for all nodes. Voltage traces $V_k(t)$ were band-pass filtered using a 1-st order bi-directional Butterworth filter in the frequency band $[0.8\Omega, 1.2\Omega]$. For each sample in the interval $t \in [7,8]$, phase values $\phi_k(t)$ were then calculated as the angle of the analytical signal. By restricting analysis to that interval we avoided transient behavior as well as possible filter artifacts. The so-determined ϕ_k contained the frequency component Ωt , which we first subtracted to obtain φ_k . Then, we opted to compute phase distributions over the time interval T and over successive trials. The (circular) mean phase, however, differed from trial to trial because of the randomly chosen initial conditions (see above). Hence for every trial we shifted phases by the mean phase of the excitatory population prior to concatenating trials. By this, the phase distributions of the excitatory phases always became centered around zero and the inhibitory phases were considered relative values. The mean phase per trial was given as

$$\Phi_{\mathcal{E}} = \arctan' \left(\frac{\sum_{k \in \mathcal{E}} \sum_{t \in T} \sin \varphi_k(t)}{\sum_{k \in \mathcal{E}} \sum_{t \in T} \cos \varphi_k(t)} \right)$$

where \arctan' denotes the quadrant-corrected inverse tangents.

The distributions displayed in the figures are the phase distributions obtained from 100 simulated trials with different initial conditions. As said, parameter values were identical across trials. For the simulations involving $C_{kl}^{(N)}$ connectivity, we used a binary form of the 66 areas parcellated Hagmann et al. matrix [24,32] as $C_{\mathcal{E}\mathcal{E}}^{(N)}$ block; see Fig 7 and 8A for the coupling scheme and $C_{\mathcal{E}\mathcal{E}}^{(N)}$, respectively. Functional connectivity was quantified as phase coherence given by $\rho_{kl} = |\langle e^{i(\phi_k(t) - \phi_l(t))} \rangle|$. We performed one hundred simulation runs of 10 s for each τ_{kl} distribution with different initial conditions and α_k, β_k and averaged the ρ_{kl} matrices over these runs. This was done to avoid high ρ_{kl} values due to common oscillation frequency alone. For each run, data in the interval $t \in [4,8]$ was used to determine ρ_{kl} . The overall coupling strengths were set to $K_1 = 1$ and $K_2 = 0.1$ for the ρ_{kl} matrices displayed in Fig 8. Structure-function correspondence $r(C_{\mathcal{E}\mathcal{E}}^{(N)}, \rho_{kl})$ was quantified as the Pearson correlation coefficient between the lower triangular parts of both matrices to avoid spurious correlation values due to common terms along the diagonal.

Eigenvalues of the linear system

To estimate the oscillatory regime of the system of coupled Freeman neural masses (1) we considered the linearized dynamics (8) for $\gamma \rightarrow \infty$ which in general reads

$$\begin{aligned} \dot{\delta V}_k &= \delta U_k \\ \dot{\delta U}_k &\approx -(\alpha_k + \beta_k) \delta U_k - \alpha_k \beta_k \delta V_k \\ &\quad + \alpha_k \beta_k \sum_{l=1}^N C_{kl} S' [V_l^{(0)}] \delta V_l(t - \tau_{kl}). \end{aligned}$$

Assuming all delays τ_{kl} to be (very) small we expanded $\delta V_l(t - \tau_{kl})$ in the sense of Taylor and approximated up to the linear order in τ_{kl} :

$$\delta V_l(t - \tau_{kl}) \approx \delta V_l(t) - \tau_{kl} \frac{d}{dt} [V_l(t)] = \delta V_l(t) - \tau_{kl} \delta U_l(t).$$

For the sake of legibility we here considered a single isolated \mathcal{E}/\mathcal{I} -pair with $C_{\mathcal{E}\mathcal{E}} = C_{\mathcal{I}\mathcal{I}} = 0$ and $C_{\mathcal{E}\mathcal{I}} = -C_{\mathcal{I}\mathcal{E}} = K_1$. We also assumed equal delays, i.e. $\tau_{kl} = \tau$. Then, we found the resulting linear dynamics as $\dot{\vec{u}} = \underline{A}\vec{u}$ where we abbreviated $\vec{u} = (\delta V_{\mathcal{E}}, \delta U_{\mathcal{E}}, \delta V_{\mathcal{I}}, \delta U_{\mathcal{I}})^T$ and

$$\underline{A} = \begin{pmatrix} 0 & 1 & 0 & 0 \\ -\alpha\beta & -(\alpha+\beta) & -\alpha\beta K_1 S' [V_{\mathcal{I}}^{(0)}] & \tau\alpha\beta K_1 S' [V_{\mathcal{I}}^{(0)}] \\ 0 & 0 & 0 & 1 \\ \alpha\beta K_1 S' [V_{\mathcal{E}}^{(0)}] & -\tau\alpha\beta K_1 S' [V_{\mathcal{E}}^{(0)}] & -\alpha\beta & -(\alpha+\beta) \end{pmatrix}.$$

The matrix \underline{A} came with eigenvalues λ_j

$$\lambda_j = -\frac{\alpha+\beta}{2} + i\frac{K_1\psi}{2}\tau \pm \frac{1}{2}\sqrt{\mp 2i\psi[(\alpha+\beta)\tau - 2K_1] + [(\alpha-\beta)^2 - K_1^2\psi^2\tau^2]};$$

where we abbreviated $\psi = \alpha\beta\sqrt{S' [V_{\mathcal{E}}^{(0)}] S' [V_{\mathcal{I}}^{(0)}]}$. These eigenvalues had the following real and imaginary parts

$$\Re\{\lambda_j\} = -\frac{\alpha+\beta}{2} \pm \frac{1}{2\sqrt{2}}\sqrt{\sqrt{[(\alpha+\beta)^2 - K_1^2\psi^2\tau^2]^2 \mp 4\psi^2[(\alpha+\beta)\tau - 2K_1]^2} + [(\alpha+\beta)^2 - K_1^2\psi^2\tau^2]}$$

$$\Im\{\lambda_j\} = \frac{K_1\psi}{2}\tau \pm \frac{1}{2\sqrt{2}}\sqrt{\sqrt{[(\alpha+\beta)^2 - K_1^2\psi^2\tau^2]^2 \mp 4\psi^2[(\alpha+\beta)\tau - 2K_1]^2} - [(\alpha+\beta)^2 - K_1^2\psi^2\tau^2]}.$$

A necessary condition for the existence of a stable limit cycle, and hence for the system (1) to display oscillatory behavior, is that the fixed point $(V_{\mathcal{E}}^{(0)}, U_{\mathcal{E}}^{(0)}, V_{\mathcal{I}}^{(0)}, U_{\mathcal{I}}^{(0)})$ is unstable. This means that for at least one of the conjugate pairs λ_j , $\Re(\lambda_j) > 0$ must hold, which was indeed the case irrespective of τ . The corresponding $\Im(\lambda_j)$ then provided a rough estimate for the frequency Ω as a function of τ , as shown in Fig 2 (solid line). In the particular case of $\tau = 0$ we found

$$\Re\{\lambda_j\}_{\tau=0} = -\frac{\alpha+\beta}{2} \pm \frac{1}{2\sqrt{2}}\sqrt{\sqrt{(\alpha-\beta)^4 + 16K_1^2\psi^2} + (\alpha-\beta)^2}$$

$$\Im\{\lambda_j\}_{\tau=0} = \pm \frac{1}{2\sqrt{2}}\sqrt{\sqrt{(\alpha-\beta)^4 + 16K_1^2\psi^2} - (\alpha-\beta)^2}.$$

revealing that for $K_1 \neq 0$ the imaginary parts did not vanish, i.e. the \mathcal{E}/\mathcal{I} -unit always displayed oscillations around the fixed point $[V_{\mathcal{E}}^{(0)}, V_{\mathcal{I}}^{(0)}]$ because the sigmoid's derivative is positive definite:

$$\Omega(\tau=0) = \frac{1}{2\sqrt{2}}\sqrt{\sqrt{(\alpha-\beta)^4 + 16\alpha^2\beta^2 K_1^2 S' [V_{\mathcal{E}}^{(0)}] S' [V_{\mathcal{I}}^{(0)}]} - (\alpha-\beta)^2}.$$

Further, for the real-part to be positive the coupling constant K_1 had to be sufficiently large and the intrinsic damping α and/or β sufficiently small but finite, because of

$$\Re\{\lambda_{1,2}\}_{\tau=0} > 0 \Leftrightarrow K_1 > \frac{\alpha+\beta}{\alpha\beta S' [V_{\mathcal{E}}^{(0)}] S' [V_{\mathcal{I}}^{(0)}]}$$

where we note that $\Re\{\lambda_{3,4}\} < 0$.

Distinct time scales

For the separation of time scales underlying all the major approximations in the current study we considered the case in which two distinct time scales are present in the system of coupled neural masses: the oscillation described by the (mean) frequency Ω and its corresponding period $2\pi/\Omega$ — from here-on referred to as fast time scale — as well as a slower time scale, on which the dynamics of ϕ_k evolve. In what follows we will verify the expression for $\dot{\phi}_k$ in (9) and show how the separation of time scales enabled us to determine the role of τ_{kl} in the convolution $W(t - \tau_{kl}) * S[V_l(t)]$. As is conventional in multiple-scaling approaches, we set the time t as 'fast' time and the 'slow' time as $\eta = \varepsilon t$ with $0 \leq \varepsilon \ll 1$. For the sake of legibility we here adopted the dot-notation for temporal derivatives d/dt and further abbreviated partial derivatives as $\frac{\partial}{\partial(\cdot)} = \hat{\partial}_{(\cdot)}$.

We denoted the deviation of the voltage from its fixed-point as $\delta V_k(t) = R_k \cos(\Omega t + \phi_k)$ where we assumed that ϕ evolved on the slow time η , i.e. $\phi_k = \phi_k(\eta)$. Note that an equivalent approach can be adopted for the amplitude dynamics, i.e. $R_k = R_k(\eta)$, which is referred to as the *slowly varying amplitude approximation*. As we were primarily interested in the ϕ_k dynamics, we regarded amplitude R_k as constant on both time scales; see *Discussion* section. By this we could readily apply the chain rule and obtained

$$\delta \dot{V}_k = \hat{\partial}_t \delta V_k + \varepsilon \hat{\partial}_\eta \delta V_k = -(\Omega + \varepsilon \hat{\partial}_\eta \phi_k) R_k \sin(\Omega t + \phi_k) = \delta U_k$$

where the last equality follows from (8). For the derivative $\delta \dot{U}_k$ we found

$$\delta \dot{U}_k = -(\Omega + \varepsilon \hat{\partial}_\eta \phi_k)^2 R_k \cos(\Omega t + \phi_k) - \varepsilon^2 \hat{\partial}_\eta^2 \phi_k R_k \sin(\Omega t + \phi_k).$$

Next we considered the expression (9) for $\dot{\phi}_k$, where we emphasize that $\dot{\phi}_k$ could here be identified as $\hat{\partial}_\eta \phi_k$, since ϕ_k evolves only on the slow time scale. To anticipate: (9) discarded all terms evolving on the fast time scale, i.e. all $\mathcal{O}(1)$ terms in favor of $\mathcal{O}(\varepsilon)$ terms and higher. To show this, recall that the right-hand side of (9) read

$$\begin{aligned}
 & -\Omega + \frac{1}{\Omega R_k^2} (\delta U_k \delta \dot{V}_k - \delta V_k \delta \dot{U}_k) \\
 = & -\Omega + \frac{1}{\Omega R_k^2} \\
 & \left[(\Omega^2 + 2\varepsilon\Omega\partial_\eta\phi_k + \varepsilon^2\partial_\eta^2\phi_k)R_k^2 - \frac{1}{2}\varepsilon^2\partial_\eta^2\phi_k R_k^2 \sin(2\Omega t + 2\phi_k) \right] \\
 & \approx 2\varepsilon\partial_\eta\phi_k + \frac{\varepsilon^2}{\Omega}\partial_\eta^2\phi_k \left(1 - \frac{1}{2}\sin(2\Omega t + 2\phi_k) \right).
 \end{aligned}$$

In words, only expressions evolving on the slow time scale were retained, i.e. only $\mathcal{O}(\varepsilon)$ and $\mathcal{O}(\varepsilon^2)$ -order terms. When focusing on the slow time scale $\mathcal{O}(\varepsilon)$ and discarding the even slower time scale $\mathcal{O}(\varepsilon^2)$, we could conclude that, up to a constant, $\dot{\phi}_k$ is given by (9); note that we here applied the so-called *two-timing* method; see, e.g., [23,69,70].

As said, we used the constancy of ϕ_k (on the fast time scale t) to evaluate the convolution term $W(t - \tau_{kl}) * S[V_l^{(0)}]$. We exploited the description in two time scales to justify the transformation of the delay τ_{kl} into phase shifts $\Omega\tau_{kl}$. We explicitly evaluated the integral $\int_{-\infty}^{t-\tau_{kl}} e^{i\Omega s} \cos(\Omega s + \phi_l) ds$ to show that (10) is its $\mathcal{O}(1)$ result. For the sake of readability we dropped the explicit time dependence of ϕ_l whenever possible.

First, by integrating by parts twice we obtained

$$\begin{aligned}
 & \int_{-\infty}^{t-\tau_{kl}} e^{i\Omega s} \cos(\Omega s + \phi_l) ds \\
 = & \frac{1}{\gamma} e^{i\Omega s} \cos(\Omega s + \phi_l) \Big|_{-\infty}^{t-\tau_{kl}} + \frac{1}{\gamma} \int_{-\infty}^{t-\tau_{kl}} (\Omega + \varepsilon\partial_\eta\phi_l) \sin(\Omega s + \phi_l) e^{i\Omega s} ds \\
 = & \frac{1}{\gamma} e^{i\Omega(t-\tau_{kl})} \cos(\Omega(t-\tau_{kl}) + \phi_l(\varepsilon(t-\tau_{kl}))) \\
 & + \frac{1}{\gamma^2} e^{i\Omega s} (\Omega + \varepsilon\partial_\eta\phi_l) \sin(\Omega s + \phi_l) \Big|_{-\infty}^{t-\tau_{kl}} \\
 & - \frac{1}{\gamma^2} \int_{-\infty}^{t-\tau_{kl}} (\Omega + \varepsilon\partial_\eta\phi_l)^2 \cos(\Omega s + \phi_l) e^{i\Omega s} ds \\
 & + \varepsilon^2 \partial_\eta^2 \phi_l \sin(\Omega s + \phi_l) e^{i\Omega s} ds.
 \end{aligned}$$

Then, when discarding $\mathcal{O}(\varepsilon^2)$ terms, we found that the integral with which we started appeared again on the right-hand side. This allowed us to write

$$\frac{\gamma^2 + \Omega^2 + 2\varepsilon\partial_\eta\phi_l}{\gamma^2} \int_{-\infty}^{t-\tau_{kl}} e^{i\Omega s} \cos(\Omega s + \phi_l) ds$$

References

1. Biswal B, Zerrin Yetkin F, Haughton VM, Hyde JS (1995) Functional connectivity in the motor cortex of resting human brain using echo-planar MRI. *Magn Reson Med* 34: 537–541.
2. Freyer F, Roberts JA, Becker R, Robinson PA, Ritter P, et al. (2011) Biophysical mechanisms of multistability in resting-state cortical rhythms. *J Neurosci* 31: 6353–6361.
3. Brookes MJ, Hale JR, Zumer JM, Stevenson CM, Francis ST, et al. (2011) Measuring functional connectivity using MEG: Methodology and comparison with fMRI. *Neuroimage* 56: 1082–1104.
4. Varela F, Lachaux JP, Rodriguez E, Martinerie J (2001) The brainweb: Phase synchronization and large-scale integration. *Nat Rev Neurosci* 2: 229–239.

$$\begin{aligned}
 & \approx \frac{1}{\gamma} \left[e^{i\Omega(t-\tau_{kl})} \cos(\Omega(t-\tau_{kl}) + \phi_l(\varepsilon(t-\tau_{kl}))) + \right. \\
 & \left. \frac{1}{\gamma} (\Omega + \varepsilon\partial_\eta\phi_l) \sin(\Omega(t-\tau_{kl}) + \phi_l(\varepsilon(t-\tau_{kl}))) \right],
 \end{aligned}$$

which resulted in

$$\begin{aligned}
 & \int_{-\infty}^{t-\tau_{kl}} e^{i\Omega s} \cos(\Omega s + \phi_l) ds \\
 = & \left(\frac{\gamma^2}{\gamma^2 + \Omega^2 + 2\varepsilon\partial_\eta\phi_l} \right) e^{i\Omega(t-\tau_{kl})} \left[\cos(\Omega(t-\tau_{kl}) + \phi_l(\varepsilon(t-\tau_{kl}))) \right. \\
 & \left. + (\Omega + \varepsilon\partial_\eta\phi_l) \sin(\Omega(t-\tau_{kl}) + \phi_l(\varepsilon(t-\tau_{kl}))) \right].
 \end{aligned}$$

With this form we could finally express the convolution terms as

$$\begin{aligned}
 W(t - \tau_{kl}) * \delta V_l(t) = & \frac{\gamma R_l}{\gamma^2 + \Omega^2 + 2\varepsilon\partial_\eta\phi_l} \left[\gamma \cos(\Omega(t - \tau_{kl}) \right. \\
 & \left. + \phi_l(\varepsilon(t - \tau_{kl}))) + (\Omega + \varepsilon\partial_\eta\phi_l) \sin(\Omega(t - \tau_{kl}) + \phi_l(\varepsilon(t - \tau_{kl}))) \right].
 \end{aligned}$$

For $\varepsilon \ll 1$ time scales are sufficiently separated to ignore all $\mathcal{O}(\varepsilon)$ terms by which we arrived at (10).

The derivation of (10) required the intuitive assumption $\phi_l(t - \tau_{kl}) \approx \phi_l(t)$, which might be motivated by a (relatively) small-delay approximation. Consider the Taylor expansion of $\phi_l(t - \tau_{kl})$ around t , which reads

$$\phi_l(t - \tau_{kl}) \approx \phi_l(t) - \frac{d}{dt} [\phi_l(t)] \tau_{kl} = \phi_l(t) - \varepsilon\partial_\eta\phi_l(t) \tau_{kl}.$$

If $\varepsilon \ll 1$ and τ_{kl} is of the order $\mathcal{O}(1)$, i.e. of the same order of magnitude as the oscillatory period $T = \frac{2\pi}{\Omega}$, then one may conclude that the approximation $\phi_l(t - \tau_{kl}) \approx \phi_l(t)$ is valid. Note that this consistent with [71]. In particular, when τ_{kl} is of order $\mathcal{O}(1/\varepsilon)$, i.e. of the same order of magnitude as the slow time scale, the approximation $\phi_l(t) \approx \phi_l(t - \tau_{kl})$ fails.

Author Contributions

Conceived and designed the experiments: RT GD AD. Performed the experiments: RT AD. Analyzed the data: RT. Contributed reagents/materials/analysis tools: RT AD. Wrote the paper: RT GD AD.

5. Bullmore E, Sporns O (2009) Complex brain networks: Graph theoretical analysis of structural and functional systems. *Nat Rev Neurosci* 10: 186–198.
6. Honey C, Sporns O, Cammoun L, Gigandet X, Thiran JP, et al. (2009) Predicting human resting-state functional connectivity from structural connectivity. *Proc Natl Acad Sci U S A* 106: 2035–2040.
7. Honey CJ, Kötter R, Breakspear M, Sporns O (2007) Network structure of cerebral cortex shapes functional connectivity on multiple time scales. *Proc Natl Acad Sci U S A* 104: 10240–10245.
8. Kandel ER, Schwartz JH, Jessell T (2000) *Principles of Neural Science*. 4th edition. New York: McGraw-Hill, Health Professions Division.
9. Roxin A, Montbrío E (2011) How effective delays shape oscillatory dynamics in neuronal networks. *Physica D* 240: 323–345.
10. Campbell S, Yuan Y, Bungay S (2005) Equivariant hopf bifurcation in a ring of identical cells with delayed coupling. *Nonlinearity* 18: 2827–2846.
11. Song Y, Makarov V, Velarde M (2009) Stability switches, oscillatory multistability, and spatiotemporal patterns of nonlinear oscillations in recurrently delay coupled neural networks. *Biol Cybern* 101: 147–167.
12. Yeung MKS, Strogatz SH (1999) Time delay in the Kuramoto model of coupled oscillators. *Phys Rev Lett* 82: 648–651.
13. Choi MY, Kim HJ, Kim D, Hong H (2000) Synchronization in a system of globally coupled oscillators with time delay. *Phys Rev E* 61: 371–381.
14. Lee WS, Ott E, Antonsen TM (2009) Large coupled oscillator systems with heterogeneous interaction delays. *Phys Rev Lett* 103: 044101.
15. Ghosh A, Rho Y, McIntosh AR, Kötter R, Jirsa VK (2008) Noise during rest enables the exploration of the brain's dynamic repertoire. *PLoS Comput Biol* 4: e1000196.
16. Deco G, Jirsa V, McIntosh AR, Sporns O, Kötter R (2009) Key role of coupling, delay, and noise in resting brain fluctuations. *Proc Natl Acad Sci U S A* 106: 10302–10307.
17. Cabral J, Hugues E, Sporns O, Deco G (2011) Role of local network oscillations in resting-state functional connectivity. *NeuroImage* 57: 130–139.
18. Deco G, Jirsa VK, Robinson PA, Breakspear M, Friston K (2008) The dynamic brain: From spiking neurons to neural masses and cortical fields. *PLoS Comput Biol* 4: e1000092.
19. Freeman W (1975) *Mass action in the nervous system*. New York: Academic Press.
20. Jansen B, Rit V (1995) Electroencephalogram and visual evoked potential generation in a mathematical model of coupled cortical columns. *Biol Cybern* 73: 357–366.
21. Robinson PA, Rennie CJ, Wright JJ (1997) Propagation and stability of waves of electrical activity in the cerebral cortex. *Phys Rev E* 56: 826–840.
22. Haken H (2004) *Synergetic computers and cognition: a top-down approach to neural nets*, volume 50. New York: Springer.
23. Guckenheimer J, Holmes P (1983) *Nonlinear oscillations, dynamical systems and bifurcations of vector fields*. Volume 42. New York: Springer-Verlag.
24. Daffertshofer A, van Wijk B (2011) On the influence of amplitude on the connectivity between phases. *Front Neuroinform* 5: 6.
25. Schuster H, Wagner P (1990) A model for neuronal oscillations in the visual cortex. *Biol Cybern* 64: 77–82.
26. David O, Kiebel SJ, Harrison LM, Mattout J, Kilner JM, et al. (2006) Dynamic causal modeling of evoked responses in EEG and MEG. *Neuroimage* 30: 1255–1272.
27. Ernst U, Pawelzik K, Geisel T (1998) Delay-induced multistable synchronization of biological oscillators. *Phys Rev E* 57: 2150–2162.
28. Ermentrout GB, Terman DH (2010) *Mathematical foundations of neuroscience*. Volume 64. New York: Springer.
29. Tass PA (2007) *Phase resetting in medicine and biology*. New York: Springer.
30. Hansel D, Mato G, Meunier C (1993) Clustering and slow switching in globally coupled phase oscillators. *Phys Rev E* 48: 3470.
31. Frank T, Daffertshofer A, Peper C, Beck P, Haken H (2000) Towards a comprehensive theory of brain activity: Coupled oscillator systems under external forces. *Physica D: Nonlinear Phenomena* 144: 62–86.
32. Hagmann P, Cammoun L, Gigandet X, Meuli R, Honey CJ, et al. (2008) Mapping the structural core of human cerebral cortex. *PLoS Biol* 6: e159.
33. Behrens T, Berg HJ, Jbabdi S, Rushworth M, Woolrich M (2007) Probabilistic diffusion tractography with multiple fibre orientations: What can we gain? *Neuroimage* 34: 144–155.
34. Fox MD, Raichle ME (2007) Spontaneous fluctuations in brain activity observed with functional magnetic resonance imaging. *Nat Rev Neurosci* 8: 700–711.
35. Vincent J, Patel G, Fox M, Snyder A, Baker J, et al. (2007) Intrinsic functional architecture in the anesthetized monkey brain. *Nature* 447: 83–86.
36. Deco G, Jirsa VK, McIntosh AR (2013) Resting brains never rest: computational insights into potential cognitive architectures. *Trends Neurosci* 36: 268–274.
37. Deco G, Jirsa VK, McIntosh AR (2011) Emerging concepts for the dynamical organization of resting-state activity in the brain. *Nat Rev Neurosci* 12: 43–56.
38. Deco G, Jirsa VK (2012) Ongoing cortical activity at rest: Criticality, multistability, and ghost attractors. *J Neurosci* 32: 3366–3375.
39. Sakaguchi H (1988) Cooperative phenomena in coupled oscillator systems under external fields. *Prog Theor Phys* 79: 39–46.
40. Strogatz S, Mirollo R (1991) Stability of incoherence in a population of coupled oscillators. *J Stat Phys* 63: 613–635.
41. Ott E, Antonsen TM (2008) Low dimensional behavior of large systems of globally coupled oscillators. *Chaos* 18: 037113.
42. Acebrón JA, Bonilla LL, Pérez Vicente CJ, Ritort F, Spigler R (2005) The Kuramoto model: A simple paradigm for synchronization phenomena. *Rev Mod Phys* 77: 137–185.
43. Wolfrum M, Omel'chenko OE, Yanchuk S, Maistrenko YL (2011) Spectral properties of chimera states. *Chaos* 21: 013112.
44. Bick C, Timme M, Paulikat D, Rathlev D, Ashwin P (2011) Chaos in symmetric phase oscillator networks. *Phys Rev Lett* 107: 244101.
45. Laing CR (2012) Disorder-induced dynamics in a pair of coupled heterogeneous phase oscillator networks. *Chaos* 22: 043104.
46. Paissan G, Zanette D (2007) Synchronization and clustering of phase oscillators with heterogeneous coupling. *Europhys Lett* 77: 20001.
47. Tass P, Haken H (1996) Synchronized oscillations in the visual cortex synergetic model. *Biol Cybern* 74: 31–39.
48. Kim S, Park SH, Ryu CS (1997) Multistability in coupled oscillator systems with time delay. *Phys Rev Lett* 79: 2911–2914.
49. Van Mieghem P (2009) A complex variant of the Kuramoto model. Technical Report 20090811, Delft University of Technology.
50. Sakaguchi H, Kuramoto Y (1986) A soluble active rotator model showing phase transitions via mutual entertainment. *Prog Theor Phys* 76: 576–581.
51. Bonilla L, Vicente CP, Rubi J (1993) Glassy synchronization in a population of coupled oscillators. *J Stat Phys* 70: 921–937.
52. Friston KJ (2011) Functional and effective connectivity: A review. *Brain Connect* 1: 13–36.
53. Stephan KE, Tittgemeyer M, Knösche TR, Moran RJ, Friston KJ (2009) Tractography-based priors for dynamic causal models. *NeuroImage* 47: 1628–1638.
54. Abrams DM, Mirollo R, Strogatz SH, Wiley DA (2008) Solvable model for chimera states of coupled oscillators. *Phys Rev Lett* 101: 084103.
55. Shanahan M (2010) Metastable chimera states in community-structured oscillator networks. *Chaos* 20: 013108.
56. Sheeba JH, Chandrasekar V, Lakshmanan M (2010) Chimera and globally clustered chimera: Impact of time delay. *Phys Rev E* 81: 046203.
57. Watts DJ, Strogatz SH (1998) Collective dynamics of small-world networks. *Nature* 393: 440–442.
58. Percha B, Dzakpasu R, Zochowski M, Parent J (2005) Transition from local to global phase synchrony in small world neural network and its possible implications for epilepsy. *Phys Rev E* 72: 031909.
59. Zhou C, Kurths J (2006) Dynamical weights and enhanced synchronization in adaptive complex networks. *Phys Rev Lett* 96: 164102.
60. Antigueira L, Rodrigues FA, van Wijk BC, da F Costa L, Daffertshofer A (2010) Estimating complex cortical networks via surface recordings a critical note. *NeuroImage* 53: 439–449.
61. Schoffelen JM, Gross J (2009) Source connectivity analysis with MEG and EEG. *Hum Brain Mapp* 30: 1857–1865.
62. Pinotsis D, Hansen E, Friston K, Jirsa V (2013) Anatomical connectivity and the resting state activity of large cortical networks. *NeuroImage* 65: 127–138.
63. Kuramoto Y (1984) *Chemical Oscillations, Waves and Turbulence*. Berlin Heidelberg: Springer-Verlag.
64. Jirsa VK (2008) Dispersion and time delay effects in synchronized spike-burst networks. *Cognitive neurodynamics* 2: 29–38.
65. Haken H (1974) *Synergetics: Basic concepts and mathematical tools*. Cooperative Effects : 1–32.
66. Strogatz SH (2000) From Kuramoto to Crawford: Exploring the onset of synchronization in populations of coupled oscillators. *Physica D: Nonlinear Phenomena* 143: 1–20.
67. Shampine LF, Thompson S (2001) Solving DDEs in Matlab. *Applied Numerical Mathematics* 37: 441–458.
68. Marreiros AC, Daunizeau J, Kiebel SJ, Friston KJ (2008) Population dynamics: Variance and the sigmoid activation function. *Neuroimage* 42: 147–157.
69. Jordan DW, Smith P (1987) *Nonlinear ordinary differential equations*. Second edition. Oxford: University Press Oxford.
70. Strogatz S (1994) *Nonlinear dynamics and chaos: with applications to physics, biology, chemistry and engineering*. Perseus Books Group.
71. Izhikevich EM (1998) Phase models with explicit time delays. *Physical Review E* 58: 905–908.